A consistent finite-strain thermomechanical quasi-nonlinear-viscoelastic viscoplastic constitutive model for thermoplastic polymers.

Ujwal Kishore Jinaga[a,], Kepa Zulueta[b], Aizeti Burgoa[b], Lucia Cobian[c,d], Ubiratan Freitas[e], Michael Lackner[f], Zoltan Major[f], Ludovic Noels[a]

[a] *Department of Aerospace and Mechanical Engineering, University of Liège, Computational & Multiscale Mechanical of Materials (CM3), Quartier Polytech 1, Allèe de la Dècouverte 9, Liège, B-4000, Belgium*
[b] *Leartiker Polymer, Xemein Hiribidea, 12 A, Biscay, Markina-Xemein, Biscay, 48270, Spain*
[c] *IMDEA Materials Institute, Calle Eric Kandel 2,Getafe, Madrid, 48270, Spain*
[d] *Department of Materials Science, E.T.S.I. de Caminos, Canales y Puertos, Universidad Politecnica de Madrid (UPM), Profesor Aranguren 3, Madrid, 28040, Spain*
[e] *cirp GmbH, Römerstraße 8, Heimsheim, 71296, Germany*
[f] *Institute of Polymer Product Engineering, Johannes Kepler University, Linz, 4040, Austria*

Abstract

Preprint submitted to International Journal of Solids and Structures (C) 2025; Licensed under the Creative Commons (CC-BY-NC-ND); formal publication on: 10.1016/j.ijsolstr.2025.113517

Thermomechanical models for thermoplastics address the highly nonlinear constitutive behaviour of semicrystalline polymers using a combination of viscoelastic and viscoplastic theories. This paper introduces a novel thermodynamically consistent quasi-non-linear thermoviscoelastic formulation in finite strain using Maxwell elements with strain-dependent moduli. The novelty encompasses the solution to the convolution integrals arising from quasi-non-linearity and the corresponding internal dissipation. This formulation is intended to produce large non-linearities in the elastic regime, including tension-compression asymmetry, which is apparent in semi-crystalline polymers subjected to thermomechanical cyclic loading. To model thermoviscoplasticity, a Drucker-Prager yield function and a Perzyna-type flow rule are considered. Additionally, reversible Mullins'-type damage as a function of the quasi-non-linear thermoviscoelastic model's deformation energy to describe the unloading response is considered. The model is formulated in a thermodynamically consistent manner by considering appropriate strain and stress measures in an intermediate configuration. For validation, this model is applied to conventional thermoplastic semicrystalline polymers, polypropylene and thermoplastic polyurethane (TPU). The experimental campaign for calibration and validation consists of Dynamic Mechanical Analyses (DMA) and

---

Email address: `l.Noels@ulg.ac.be` (Ludovic Noels)

uniaxial monotonic and cyclic tests in tension and compression. To further elucidate the applicability of this model, validation is performed by comparing numerical results to experimental performance under torsion of 3D-printed TPU specimens at varying strain rates.

Keywords - Quasi-non-linear thermoviscoelasticity, Strain-dependent moduli, Thermoviscoplasticity, Reversible Mullins'-type damage, Dynamic Mechanical Analyses

1. Introduction

Thermoplastic polymers offer high strength-to-weight ratio, bio-affinity and recyclability among other advantages and consequently have found applications in aerospace, automobile and biomechanical industries. Their remoulding property due to reversible glass transition in a temperature range starkly contrasts thermoset polymers. Experimental data on thermoplastic polymers with varying degrees of crystallinity suggest high sensitivity to strain rates, temperatures and even stress states [1, 2]. On a temperature scale, this constitutive response comprises of a brittle glassy state at lower temperatures and a ductile rubbery state at higher temperatures. For semicrystalline polymers, see [3], this brittle to ductile transition is highly pronounced and the onset of yielding is higher at lower temperatures. The sensitivity to strain rates tends to produce a similar but opposing trend to temperature, where the constitutive response at a higher strain rate corresponds to that of a lower temperature [4]. The stress state tends to influence the mechanical response of thermoplastic polymers in both elastic and plastic regimes. Elastic moduli are found to vary in tension and compression tests as shown by [2] for an amorphous polymer, [5] for semi-crystalline polymers, and [6] for soft-polymers. This asymmetry in moduli is perhaps related to the extension of microstructural pores under tensile loading that lowers the material stiffness in tension [5]. However, this is pure conjecture and the only conclusive finding concerning such asymmetry, if any, is that it varies with temperature [5]. Initial yield stresses exhibit a similar characteristic as summarised for various thermoplastic polymers in [7]. The rate-dependent yielding stage is known to be dependent on hydrostatic pressure [8], and is followed by the characteristic post-peak softening for amorphous polymers at low temperatures that is less pronounced at high temperatures [9] and for an increasing degree of crystallinity, see [3]. Higher strain rates lead to further hardening post-yielding. In general, the rate-dependency, i.e., the viscous nature of the polymer, results in self-heating due to a majority of the mechanical energy being converted to heat [10]. Naturally, temperature-induced softening is a concern and competes with plastic hardening [11]. Equally captivating is the response to cyclic loading which exhibits hysteresis loops indicating energy dissipation [12]. In cyclic loading of elastomers exhibiting rubber-like properties, as is also the case at temperatures higher than that of glass transition in generic thermoplastic polymers, the mechanical response is influenced by a Mullins'-like effect where the stress response in successive reloads is of a lower value and is a function of the maximum load encountered previously in the loading history [13, 14]. For a semi-crystalline thermoplastic polymer subjected to monotonic deformation, regions of varying crystallinity exhibit distinct strain-rate and temperature dependent phenomena as discussed in [11]. Under cyclic deformation, depending on the strain level, load-unload cycles subject the molecular chains to breaking and restoration, pointing at energy hysteresis in successive cycles [14].

Constitutive laws of this thermomechanical response can be broadly classified into physical and phenomenological models, where the former are motivated by the contributions of the amorphous and crystalline phases to the material response, and the latter regard the material as a homogeneous medium exhibiting individual phenomena such as viscoelasticity and viscoplasticity. Numerous physical models have been developed to address the later stages of hardening and reorientation in amorphous thermoplastics [15], using Eyring dashpots and Langevin springs to describe intermolecular and molecular level interactions so as to evaluate large deformation stress response and dissipation, accounting for pressure, strain-rate and temperature dependencies across various temperature ranges [16, 17] and have been further developed for semicrystalline polymers to include the Mullins' effect, crystalline contributions, self-heating, and non-isothermal behaviors [18, 19, 11]. Recent advancements include the modelling of double yield phenomenon in semicrystalline polymers to analyse the amorphous and crystalline phase contributions to yielding [20] and a large deformation model based on [17] to capture the evolution of crystallinity for arbitrary thermal processing conditions using nonlinear kinematic and isotropic hardening with tension-compression yield asymmetry and pressure-dependent yielding [21]. Despite model parameters carrying physical significance, application of physical models to an arbitrary polymer can be challenging as the molecular kinetics of deformation can change significantly across wide temperature ranges [11] and consequently, such models may require thorough specialisation for a given semicrystalline polymer, especially since the physics of tension-compression asymmetry in elasticity remains unclear [5].

Phenomenological modelling is extensively used to analyse semicrystalline thermoplastic polymers with various phenomenological regimes as roughly identified with varying temperature in Fig. 1. To rheologically characterise viscoelastic response, models utilising stress relaxation data through a combination of springs and dashpots are popular to show nonlinear response such as the generalized Maxwell model in [22] , generalized Kelvin model in [23] or similar constructions with springs and dashpots reported in [24]. To account for strain-induced nonlinearities, stress relaxation has been combined with strain dependency of the time-dependent relaxation modulus [25]. This has been applied in biomechanical models of small strains [26] and finite strains [27], but not in polymers. Elastic-viscoplastic models have been adapted from constitutive laws of metals based

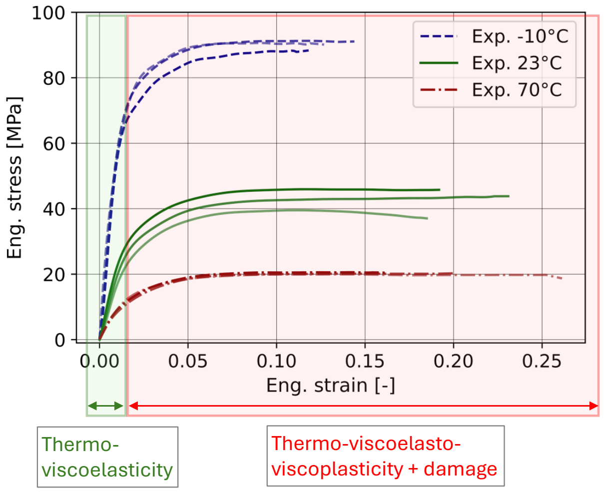

Figure 1: Thermomechanical response of a thermoplastic polymer with varying temperature.

on the overstress model [28] and generalized yield criteria with pressure and J3-invariants [7] for generic polymers. This generic viscoplasticity has been combined with viscoelastic models (VEVP models) for isotropic polymers of varying chemical constituencies, isothermally [22, 23, 29], and non-isothermally [30, 31, 32], of which [22, 29, 32] consider pressure-dependent viscoplastic yield criteria, whereas, the rest consider only the J2-invariant in their respective yield functions. Krairi and co-workers [31] have also captured self-heating due to thermoviscoplasticity and hardening but do not consider cyclic loading. Recently, a VEVP model for a semi-crystalline polymer in monotonic loading, has been developed with the viscoplastic part, which in addition to traditional viscous kinematic hardening, consists of pseudo-viscous non-linear kinematic hardening motivated by dislocation and slip processes to model the orientation hardening stage, but only at constant temperature [33]. Also of note is the model of [34] for rate-dependent soft materials where tension-compression asymmetry using a bi-phasic modulus has been considered, albeit, with a slope discontinuity. This elastic asymmetry largely remains unaddressed even in phenomenological models. Elsewhere, pseudo-elastic models for filled rubbers and elastomers have been extensively used to model the Mullins' effect, see the review of [35], and more recently, a fully thermomechanically consistent model [36] and an isothermal hyperelastic-viscoplastic model with Maxwell elements for Mullins' effect with a permanent set [37]. However a generalised thermomechanically consistent VEVP model with Mullins' effect as a dissipative process for cyclic loading in thermoplastic polymers is lacking. Additionally, viscoelastic models using relaxation spectra employ convolution integrals to evaluate the stress response involving the addition of terms across time-steps [38], which in the finite strain regime, leads to a loss of coaxiality of the stress and strain tensors expressed in the intermediate configuration resulting in inconsistent definitions of stress power for an isotropic material [39]. With a view of ensuring thermodynamic consistency, an alternative strain definition was implemented in [29] which leads to straightforward but cumbersome definitions of the rate of the strain tensor.

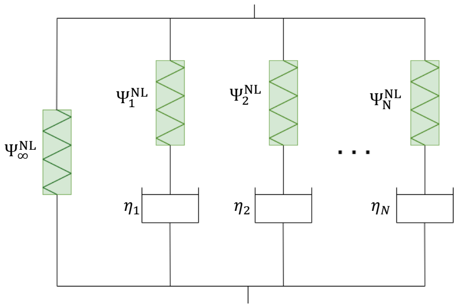

Figure 2: The Quasi-nonlinear Maxwell model: Ψ_i^{NL} is the highly nonlinear free energy of a spring with strain-dependent modulus and η_i is the viscosity of the Newtonian dashpot.

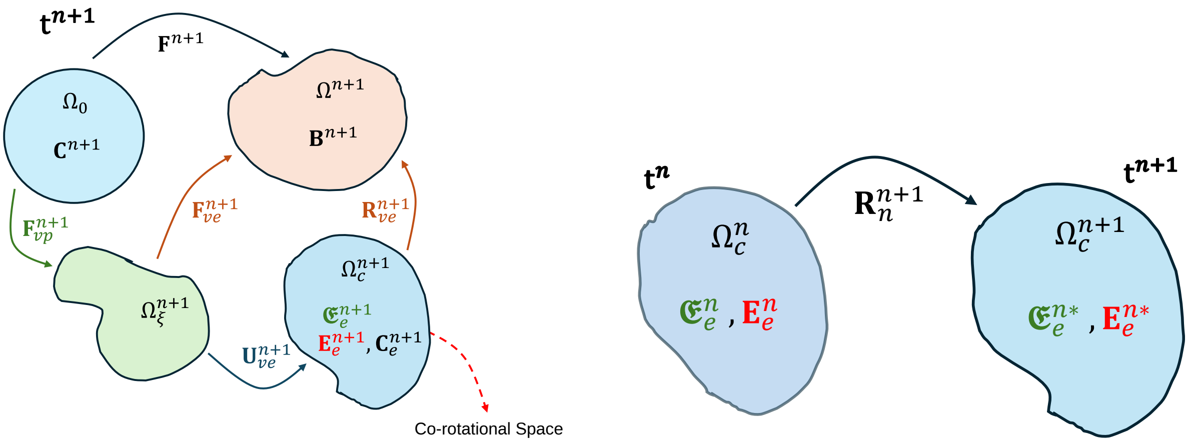

(a) (b)

Figure 3: Configurations: (a) Material, intermediate (or relaxed) and co-rotational configurations, respectively Ω_0, Ω_ξ^{n+1} and Ω_c^{n+1}, defining the multiplicative decomposition of the deformation gradient; (b) Tensors in the co-rotational configuration at two subsequent time-steps transformed for coaxiality.

To address the aforementioned limitations of the existing constitutive models, the present work develops a thermodynamically consistent finite-strain constitutive model for isotropic thermoplastic polymers to capture: i) strain-induced nonlinearities, in particular the tension-compression asymmetry, in both viscoelastic and viscoplastic ranges; ii) thermomechanical coupling, with in particular a time-temperature equivalence [40, 31] in the viscoelastic range and temperature-dependent asymmetric tension-compression yield strengths and viscosity in the viscoplastic range; and iii) reversible, and inherently rate and temperature-dependent, Mullins'-type effect. To this end, the following novel key ingredients are introduced:

1. Thermoviscoelasticity is modelled using a generalized Maxwell model with strain-dependent moduli inducing nonlinear hyperelastic response to produce a sigmoid-like stress-strain curve for a typical thermoplastic polymer. This is unlike the polynomial functions used in [26,

27]. This so-called quasi-nonlinear (QNL) viscoelasticity, owing to the combination of linear viscoelasticity and non-linear strain dependency, is illustrated in Fig. 2.

2. The QNL formulation allows the implementation of tension-compression, i.e., stress-state-dependent parameters as a function of the trace of the strain tensor to model asymmetric moduli.

3. Following [22], the pressure-dependent viscoplastic response is written in the co-rotational space Ω_c^{n+1}, see Fig. 3a, and Fig. 3b where a suitable transformation involving a rotation matrix is introduced to rotate the strain tensors of the previous configuration into the current configuration for consistent definitions of plastic driving stress, allowing to recover thermodynamical consistency.

4. In temperature-dependent thermoviscoelasticity, it is typical to perform the convolution integrals in reduced or material time, [41], where an Arrhenius-type equation is applied to utilise the time-temperature superposition principle [42]. We adopt herein the time-temperature equivalence in thermoviscoelasticity [40, 31]. In thermoviscoplasticity, the asymmetric tension-compression yield strengths and viscosity are made temperature-dependent using negative-exponential-like functions, following [31].

5. Following the thermodynamic foundation for a continuum damage scalar, see [43], this study introduces an idealised and completely dissipative Mullins'-like effect towards developing a generalized VEVP-Mullins' constitutive model for polymers. In this context, idealised refers to the neglect of a permanent set associated with Mullins' effect [14] and is modelled as a reversible damage-like variable.

The article is outlined as follows: Section 2 presents the kinematics of large deformations and thermomechanically consistent formulations of stress and dissipation arising from all the mechanisms considered in this study; Section 3 presents the quasi-nonlinear thermoviscoelastic model and introduces the transformation to restore coaxiality of the plastic driving stress; Section 4 elaborates on the thermodynamic foundation for the viscoplastic model developed in [22], extends it to include the Chaboche non-linear kinematic hardening modulus formulation [44] and summarises the thermomechanical constitutive equations; Section 5 provides the experimental campaign and characterisation for the constitutive model parameters for 2 different kinds of thermoplastic polymers which exhibit different thermomechanical responses - polypropylene (PP) and thermoplastic polyurethane (TPU); Section 6 reports the numerical performance of the model in comparison with the experimental data and corresponding discussions; and Section 7 concludes this study with insights and possible future extensions.

2. Kinematics and Thermodynamics

2.1. Kinematics

For a homogeneous body B in the current configuration, with its corresponding reference configuration B_0, the deformation gradient $\mathbf{F}$ is defined as the one-to-one mapping

$$\mathbf{F} = \frac{\partial \boldsymbol{x}}{\partial \boldsymbol{X}} \ , \tag{1}$$

which has a strictly positive Jacobian, i.e., $J = \det \mathbf{F} > 0$. For finite deformation plasticity, the multiplicative decomposition is adopted as below:

$$\mathbf{F} = \mathbf{F}_e \mathbf{F}_p \ \ . \tag{2}$$

The thermal dilatation effect is considered within $\mathbf{F}_e$. The Hencky strain tensor, $\mathbf{E}$, is adopted as the strain measure defined below along with its spectral representation:

$$\mathbf{E} = \frac{1}{2} \ln \mathbf{C} = \frac{1}{2} \sum_{m=1}^{3} \ln \lambda_m \, \mathbf{G}_m \otimes \mathbf{G}_m \ . \tag{3}$$

where the eigenvalues λ_m, and the bases, $\mathbf{G}_m \otimes \mathbf{G}_m$ belong to those of $\mathbf{C} = \mathbf{F}^T \mathbf{F}$.

2.2. Thermodynamical consistency

The Energy Balance per unit reference volume, i.e., the 1^{st} law of thermodynamics in the reference configuration, is presented below in the strong form:

$$\dot{E}(\boldsymbol{X}, T) = -\mathrm{Div}\, \boldsymbol{Q} + R_{\mathrm{ext}} + \mathbf{P} : \dot{\mathbf{F}} \ , \tag{4}$$

where E is the internal energy and $\boldsymbol{Q}$ is the heat flux vector in the reference configuration; T is the temperature; R_{ext} is the external volumetric heat source per unit reference volume, and $\mathbf{P}$ is the 1^{st} PK stress tensor. The strong form of the Principle of Irreversibility, 2^{nd} law of thermodynamics, is given below as

$$\varrho = \dot{S}(\boldsymbol{X}, T) + \mathrm{Div}\, \frac{\boldsymbol{Q}}{T} - \frac{R_{\mathrm{ext}}}{T} \geq 0 \ , \tag{5}$$

where S is the entropy per unit reference volume; ϱ is the entropy production per unit reference volume that must be ≥ 0 and the other two terms are the negative of entropy supply.

The Helmholtz Free Energy (ψ) is defined as follows:

$$\psi = E - TS \ . \tag{6}$$

In generalized thermoviscomechanics, the independent and dependent variables can be expressed as $\left(\mathbf{E}_e, T, \boldsymbol{H}; \boldsymbol{\beta}_j, \widehat{\psi}_{\max}\right)$ and $(\psi, \mathbf{P}, S, \boldsymbol{Q})$, respectively, where $\mathbf{E}_e$ is the Hencky strain in the intermediate configuration; $\boldsymbol{H}$ is the temperature gradient in the reference configuration; $\boldsymbol{\beta}_j$ is the vector of internal variables specialised as $\boldsymbol{\beta}_{j=1,2,3} = \{\boldsymbol{\Gamma}_i, \boldsymbol{\alpha}, r\}$, such that the internal variable $\boldsymbol{\Gamma}_i$ is the viscous strain in the dashpot of the i^{th} element of the Generalized Maxwell Model in thermoviscoelasticity, see Fig. 2, in thermoviscoplasticity, $\boldsymbol{\alpha}$ is the backstrain tensor and r is the scalar isotropic hardening variable; and lastly, $\widehat{\psi}_{\max}$ is the internal variable of Mullins' effect defined as the maximum deformation energy achieved in the loading history of a supposed undamaged configuration associated with the (pseudo-)damaged configuration where ψ exists. $\widehat{\psi}_{\max}$ is defined as follows:

$$\widehat{\psi}_{\max} = \max\{\widehat{\psi}(\tau), \tau \leq t\} \; , \tag{7}$$

where $\widehat{\psi}$ is the free energy in the undamaged configuration. The free energy ψ in the (pseudo-)damaged configuration reads

$$\psi = \psi\left(\widehat{\psi}\left(\mathbf{E}_e, T, \boldsymbol{H}; \boldsymbol{\beta}_{j=1,2,3} = \{\boldsymbol{\Gamma}_i, \boldsymbol{\alpha}, r\}\right), \widehat{\psi}_{\max}\right) \; , \tag{8}$$

where all the dissipative processes are prescribed in the undamaged configuration except that of Mullins' effect. To produce the Mullins' effect, a state variable (ζ) model is chosen, where $\zeta \in [0,1]$ and is a function of the maximum load previously recorded in the loading history as $\zeta = \zeta\left(\widehat{\psi}, \widehat{\psi}_{\max}\right)$, where $\zeta = 1$ for primary loading and $\zeta \leq 1$ for un-/reloading [35]. This is used to redefine the free energy as follows:

$$\psi(\widehat{\psi}, \widehat{\psi}_{\max}) = \int_0^{\widehat{\psi}} \zeta(\upsilon, \widehat{\psi}_{\max}) \, d\upsilon \; , \tag{9}$$

allowing the following convenient rate form:

$$\dot{\psi} = \frac{\partial \psi}{\partial \widehat{\psi}} \dot{\widehat{\psi}} + \frac{\partial \psi}{\partial \widehat{\psi}_{\max}} \dot{\widehat{\psi}}_{\max} = \zeta \dot{\widehat{\psi}} + \frac{\partial \psi}{\partial \widehat{\psi}_{\max}} \dot{\widehat{\psi}}_{\max} \; , \tag{10}$$

where $\zeta = \frac{\partial \psi}{\partial \widehat{\psi}}$ is used. Through Eq. (8), the rate form of $\widehat{\psi}$ is as follows:

$$\dot{\widehat{\psi}} = \frac{\partial \widehat{\psi}}{\partial \mathbf{E}_e} : \dot{\mathbf{E}}_e(t) + \frac{\partial \widehat{\psi}}{\partial T} \dot{T}(t) + \frac{\partial \widehat{\psi}}{\partial \boldsymbol{H}} \cdot \dot{\boldsymbol{H}}(t) + \sum_j \frac{\partial \widehat{\psi}}{\partial \boldsymbol{\beta}_j} : \dot{\boldsymbol{\beta}}_j(t) \; . \tag{11}$$

The entropy production per unit reference volume (ϱ) is rewritten to eliminate the external heat source, R_{ext}, by combining Eqs. (4) and (5), and then Eq. (6), yielding

$$\varrho = T\dot{S} + \mathbf{P} : \dot{\mathbf{F}} - \dot{E} - \frac{1}{T}\boldsymbol{Q} \cdot \boldsymbol{H} = -\dot{\psi} - S\dot{T} + \mathbf{P} : \dot{\mathbf{F}} - \frac{1}{T}\boldsymbol{Q} \cdot \boldsymbol{H} \geq 0 \; . \tag{12}$$

This is the more familiar form of the Clausius-Duhem Inequality (CDI) that is considered a-priori to formulate all constitutive equations such that no thermomechanical process may violate it. Then, the rate forms in Eqs. (10) and (11) are substituted above and rearranged to obtain the following:

$$\left(\mathbf{P}:\dot{\mathbf{F}} - \zeta \frac{\partial\widehat{\psi}}{\partial \mathbf{E}_e} : \dot{\mathbf{E}}_e\right) - \left(S + \zeta\frac{\partial\widehat{\psi}}{\partial T}\right)\dot{T} - \zeta\frac{\partial\widehat{\psi}}{\partial \boldsymbol{H}}\cdot\dot{\boldsymbol{H}} - \zeta\sum_j \frac{\partial\widehat{\psi}}{\partial\boldsymbol{\beta}_j}:\dot{\boldsymbol{\beta}}_j - \frac{\partial\psi}{\partial\widehat{\psi}_{\max}}\dot{\widehat{\psi}}_{\max} - \frac{1}{T}\boldsymbol{Q}\cdot\boldsymbol{H} \;\geq\; 0\,. \tag{13}$$

Firstly, $\widehat{\psi}$ and therefore ψ are independent of $\boldsymbol{H}$ as $\frac{\partial\widehat{\psi}}{\partial\boldsymbol{H}}\cdot\dot{\boldsymbol{H}} = 0$ and secondly, the independent heat flux term, $-\frac{1}{T}\boldsymbol{Q}\cdot\boldsymbol{H} \geq 0$, implies a minima on itself. Using Fourier's Law of heat conduction in the reference configuration,

$$\boldsymbol{Q} = -J\left(\mathbf{F}^{-1}\cdot\boldsymbol{\chi}\cdot\mathbf{F}^{-T}\right)\cdot\boldsymbol{H}\,, \tag{14}$$

the conditions discussed above restrict the thermal conductivity matrix $\boldsymbol{\chi}$ to a semi-positive definite tensor. Consequently, χ is a positive scalar for an isotropic material with $\boldsymbol{\chi} = \chi\mathbf{I}$, where $\mathbf{I}$ is the 2nd order identity tensor. Before proceeding, it is useful to note the revised dependencies of the deformation energy in the undamaged state split into thermoviscoelastic and thermoviscoplastic parts using $\boldsymbol{\beta}_j$:

$$\widehat{\psi} = \widehat{\psi}_{ve}(\mathbf{E}_e, T, \boldsymbol{\Gamma}_i) + \widehat{\psi}_{vp}(T, \boldsymbol{\alpha}, r)\,. \tag{15}$$

For further development, the prefix "thermovisco" is dropped for brevity and the stress power is broken into elastic and plastic components using Eq. (2) and referring to [45]:

$$\mathbf{P}:\dot{\mathbf{F}} = \mathbf{P}:\dot{\mathbf{F}}_e\mathbf{F}_p + \mathbf{P}:\mathbf{F}_e\dot{\mathbf{F}}_p = \underbrace{\frac{1}{2}\mathbf{S}_e:\dot{\mathbf{C}}_e}_{\text{Elastic Power}} + \underbrace{\mathbf{M}_e:\mathbf{L}_p}_{\text{Plastic Power}}\,. \tag{16}$$

In the above equation, $\mathbf{S}_e$ is the 2^{nd} PK stress, $\mathbf{M}_e$ is the Mandel stress and $\mathbf{L}_p$ is the spatial rate of plastic deformation, all of which are tensors defined in the intermediate configuration. The Mandel stress is related to 2^{nd} PK stress as: $\mathbf{M}_e = \mathbf{C}_e\mathbf{S}_e$. Then, using the first half of Eq. (16) and eliminating the heat flux term, Eq. (13) is rewritten as:

$$\left(\mathbf{P}:\dot{\mathbf{F}}_e\mathbf{F}_p - \zeta\frac{\partial\widehat{\psi}}{\partial\mathbf{E}_e}:\dot{\mathbf{E}}_e\right) + \left(\mathbf{P}:\mathbf{F}_e\dot{\mathbf{F}}_p - \zeta\sum_{j=1}^{3}\frac{\partial\widehat{\psi}}{\partial\boldsymbol{\beta}_j}:\dot{\boldsymbol{\beta}}_j - \frac{\partial\psi}{\partial\widehat{\psi}_{\max}}\dot{\widehat{\psi}}_{\max}\right) - \left(S + \zeta\frac{\partial\widehat{\psi}}{\partial T}\right)\dot{T} \geq 0\,. \tag{17}$$

The first term gives the thermodynamic definition of the stress tensor:

$$\mathbf{P}:\dot{\mathbf{F}}_e\mathbf{F}_p = \zeta\frac{\partial\widehat{\psi}}{\partial\mathbf{E}_e}:\dot{\mathbf{E}}_e = \zeta\frac{\partial\widehat{\psi}}{\partial\mathbf{C}_e}:\dot{\mathbf{C}}_e\,, \tag{18}$$

where the conversion stems from the log strain $\mathbf{E}_e$ in Eq. (3). It is however convenient to define the stress tensors in the undamaged state where strain tensor conversions hold similarly, leading to:

$$\mathbf{P}:\dot{\mathbf{F}}_e\mathbf{F}_p = \zeta\frac{\partial\widehat{\psi}}{\partial\mathbf{C}_e}:\dot{\mathbf{C}}_e = 2\,\zeta\,\mathbf{F}_e\frac{\partial\widehat{\psi}}{\partial\mathbf{C}_e}\mathbf{F}_p^{-T}:\dot{\mathbf{F}}_e\mathbf{F}_p = \zeta\widehat{\mathbf{P}}:\dot{\mathbf{F}}_e\mathbf{F}_p\,. \tag{19}$$

Similar to this relation, the conjugacy relationships of the 2^{nd} PK stress $\widehat{\mathbf{S}}_e$ with $\mathbf{C}_e$ and the co-rotational Kirchhoff stress $\widehat{\boldsymbol{\tau}}_e$ with $\mathbf{E}_e$, i.e., $2\frac{\partial\widehat{\psi}}{\partial\mathbf{C}_e} = \widehat{\mathbf{S}}_e$ and $\frac{\partial\widehat{\psi}}{\partial\mathbf{E}_e} = \widehat{\boldsymbol{\tau}}_e$, respectively, and the Mandel stress, $\widehat{\mathbf{M}}_e = \mathbf{C}_e\widehat{\mathbf{S}}_e$, are noted.

Eventualy, the damage-scaled consistent definition of the 1^{st} PK stress is written:

$$\mathbf{P} = \zeta \widehat{\mathbf{P}} \; . \tag{20}$$

Then, the third term of Eq. (17) defines entropy per unit reference volume (S) and equivalently, expressed in terms of entropy in the undamaged state:

$$S = -\zeta \frac{\partial \widehat{\psi}}{\partial T} \quad \text{and} \quad S = \zeta \widehat{S} \; . \tag{21}$$

Finally, using the definition of plastic power in Eq. (16) in the undamaged state, the mechanical dissipation inequality (δ) reaches its new form:

$$\delta \equiv \underbrace{\zeta \left(\widehat{\mathbf{M}}_e : \mathbf{L}_p - \sum_j \frac{\partial \widehat{\psi}}{\partial \boldsymbol{\beta}_j} : \dot{\boldsymbol{\beta}}_j \right)}_{\widehat{\delta}} - \frac{\partial \psi}{\partial \widehat{\psi}_{\max}} \dot{\widehat{\psi}}_{\max} \geq 0 \; , \tag{22}$$

where, $\mathbf{L}_p = \dot{\mathbf{F}}_p \mathbf{F}_p^{-1}$ is the rate of plastic deformation in the intermediate configuration. The terms in the brackets are realised as the mechanical dissipation inequality in the undamaged state, $\widehat{\delta}$, the first term of which is the (thermovisco)plastic power and the remaining terms give restrictions on the corresponding internal variables; ζ is a positive scalar by definition. Assuming that $\widehat{\delta}$ individually satisfies the inequality in the undamaged state, i.e., $\widehat{\delta} \geq 0$, the last term, using Eq. (9) and imposing that ζ is a continuous and differentiable function of $\widehat{\psi}$, leads to the condition:

$$\frac{\partial \zeta}{\partial \widehat{\psi}_{\max}} \leq 0 \; . \tag{23}$$

Then, the function for the Mullins' state variable, ζ, is explicitly stated here:

$$\zeta = 1 - z \left(1 - \frac{\widehat{\psi}}{\widehat{\psi}_{\max}} \right) \; , \tag{24}$$

where z is a parameter to be calibrated later and can be made temperature-dependent in the form $z = z_0 \, a_{T_\zeta}$ where a_{T_ζ} is a scalar function of temperature, the shape of which is defined later. The condition stated in Eq. (23) is satisfied for $z \in [0, 1)$.

2.3. Self Heating

To evaluate the heat dissipated because of inelastic processes and Mullins'-like effect, the corresponding equations of the internal energy in Eq. (4) and the time derivative of $\widehat{\psi}$ in Eq. (6) in the (pseudo-)damaged state are combined to recast the time derivative of entropy as follows:

$$T \dot{S} = -\mathrm{Div} \boldsymbol{Q} + R_{\text{ext}} + \delta \; , \tag{25}$$

where the time derivative of $\dot{S} = -\frac{\partial \dot{\psi}}{\partial T}$ is elaborated below using Eq. (10) first and then the temperature derivative of Eq. (11):

$$\dot{S} = -\frac{\partial \zeta}{\partial T} \dot{\widehat{\psi}} - \zeta \left(\frac{\partial^2 \widehat{\psi}}{\partial T^2} \dot{T} + \frac{\partial^2 \widehat{\psi}}{\partial T \partial \mathbf{E}_e} : \dot{\mathbf{E}}_e + \sum_{j=1}^{3} \frac{\partial^2 \widehat{\psi}}{\partial T \partial \boldsymbol{\beta}_j} : \dot{\boldsymbol{\beta}}_j \right) - \frac{\partial^2 \psi}{\partial T \partial \widehat{\psi}_{\max}} \dot{\widehat{\psi}}_{\max} \; . \tag{26}$$

This relation is substituted in Eq. (25) and then, using Eq. (22) written in terms of the heat flux term $\mathrm{Div}\,\boldsymbol{Q}$ to give:

$$
\begin{aligned}
\mathrm{Div}\,\boldsymbol{Q} \quad &= \quad R_{\mathrm{ext}} + \zeta\left(T\frac{\partial^2\widehat{\psi}}{\partial T^2}\right)\dot{T} + \; ... \\
... \quad &+\zeta\left(\widehat{\mathbf{M}}_e : \mathbf{L}_p + T\frac{\partial}{\partial T}\left(\frac{\partial\widehat{\psi}}{\partial \mathbf{E}_e}\right) : \dot{\mathbf{E}}_e - \sum_{j=1}^{3}\frac{\partial}{\partial \boldsymbol{\beta}_j}\left(\widehat{\psi} - T\frac{\partial\widehat{\psi}}{\partial T}\right) : \dot{\boldsymbol{\beta}}_j\right) + \; ... \\
... \quad &+T\frac{\partial\zeta}{\partial T}\dot{\widehat{\psi}} - \left(\frac{\partial\psi}{\partial\widehat{\psi}_{\max}} - T\frac{\partial^2\psi}{\partial T\partial\widehat{\psi}_{\max}}\right)\dot{\widehat{\psi}}_{\max}\,,
\end{aligned}
\tag{27}
$$

where the 2^{nd} term on the right-hand side gives the specific heat at constant deformation:

$$
C_d = -\zeta T\frac{\partial^2\widehat{\psi}}{\partial T^2}\,. \tag{28}
$$

Then, the term $T\frac{\partial}{\partial T}\left(\frac{\partial\widehat{\psi}}{\partial \mathbf{E}_e}\right) : \dot{\mathbf{E}}_e$ denotes the thermoelastic heat or the Gough-Joule effect that leads to the increment/decrement in temperature due to compressive/tensile loading respectively. The terms $\sum_j \frac{\partial}{\partial\boldsymbol{\beta}_j}\left(-T\frac{\partial\widehat{\psi}}{\partial T}\right) : \dot{\boldsymbol{\beta}}_j$ and $T\frac{\partial^2\widehat{\psi}}{\partial T\partial\widehat{\psi}_{\max}}\dot{\widehat{\psi}}_{\max}$ are the temperature dependencies of the dissipation pertaining to inelastic phenomena (thermoviscoelasticity and thermoviscoplasticity), and Mullins'-like effect respectively, that are not considered in the current study. The term $T\frac{\partial\zeta}{\partial T}\dot{\widehat{\psi}}$ is the thermal coupling of the Mullins'-like effect and is also ignored. Finally, since the left-hand side is equivalent to a heat source, albeit one that is generated by mechanical dissipation and therefore produces material self-heating, it is written as the mechanical source (W_M), i.e., $W_M = \mathrm{Div}\,\boldsymbol{Q}$ and is rewritten to retain the relevant terms below:

$$
W_M = \zeta\left(-C_d\dot{T} + \widehat{\mathbf{M}}_e : \mathbf{L}_p + T\frac{\partial}{\partial T}\left(\frac{\partial\widehat{\psi}}{\partial\mathbf{E}_e}\right) : \dot{\mathbf{E}}_e - \sum_j\frac{\partial\widehat{\psi}}{\partial\boldsymbol{\beta}_j} : \dot{\boldsymbol{\beta}}_j\right) + R_{\mathrm{ext}} - \frac{\partial\psi}{\partial\widehat{\psi}_{\max}}\dot{\widehat{\psi}}_{\max}\,. \tag{29}
$$

3. Thermoviscoelasticity

Large non-linearities are captured using strain-dependent moduli in all Maxwell branches within a hyperelastic foundation and the time-temperature superposition principle, and the tension-compression asymmetry in elastic moduli through a regularisation parameter. The hyperelastic foundation is first developed for an isothermal 1D Quasi-Nonlinear Maxwell Element and then generalized for its 3D counterpart.

3.1. 1D Quasi-Nonlinear Maxwell Element

The first step is to develop relations for the free energy ($\widehat{\psi}_{1\mathrm{D}}$) and mechanical dissipation ($\hat{\delta}_{1\mathrm{D}}$) for a simple case of an isothermal Maxwell element. The 1D co-rotational Kirchhoff stress in this element is $\widehat{\tau}$ and the total strain of the element is ϵ. The internal variable is the strain-like contribution of the dashpot, ϵ_v. Since the strains are additive in a branch, the strain in the branch spring (ϵ_s) is the function of the total strain and the internal variable, i.e., $\epsilon_s = \epsilon - \epsilon_v$. The modulus of the spring is then defined as the function of its strain, i.e., $E = E(\epsilon_s)$. The viscosity of the dashpot, η, has the general relation, $\eta = E\,\kappa$, where κ is the time constant. Finally, using the assumption of linear viscoelasticity, implying quadratic dissipation, and noting that stress across the spring and the dashpot are equivalent, the following stress relation holds:

$$\widehat{\tau} = E(\epsilon_s)\,\epsilon_s = \eta\,\dot{\epsilon}_v \; . \tag{30}$$

From hyperelasticity, $\widehat{\tau} = \frac{\partial \widehat{\psi}_{1\mathrm{D}}}{\partial \epsilon_s}$, which results in the free energy having the hyperelastic form:

$$\widehat{\psi}_{1\mathrm{D}} = \int_0^{\epsilon_s} \widehat{\tau}\, d\epsilon_s = \int_0^{\epsilon_s} E(\epsilon_s)\,\epsilon_s\, d\epsilon_s \; , \tag{31}$$

which is easily solved for an analytically integrable function of $E(\epsilon_s)\,\epsilon_s$. Also, since $\epsilon_s = \epsilon - \epsilon_v$, $\frac{\partial \widehat{\psi}_{1\mathrm{D}}}{\partial \epsilon_v} = -\widehat{\tau}$, which is the expected energy conjugation relationship in linear viscoelastic theory. Then, the quadratic internal dissipation due to the evolution of the viscoelastic internal variable has the following recognisable form, based on Eq. (22):

$$\hat{\delta}_{1\mathrm{D}} = -\frac{\partial \widehat{\psi}_{1\mathrm{D}}}{\partial \epsilon_v}\,\dot{\epsilon}_v = \widehat{\tau}\dot{\epsilon}_v = \frac{\widehat{\tau}^2}{E(\epsilon_s)\,\kappa} \geq 0 \; , \tag{32}$$

resulting in the condition for thermodynamical consistency $\kappa > 0$.

Writing the Eq. (30) in terms of ϵ_s leads to:

$$\epsilon_s = \frac{E(\epsilon_s)\kappa}{E(\epsilon_s)}\,\frac{d}{dt}(\epsilon - \epsilon_s) \; , \tag{33}$$

allowing the recovery of the classical ordinary differential equation (ODE):

$$\dot{\epsilon}_s + \frac{\epsilon_s}{\kappa} = \dot{\epsilon} \; . \tag{34}$$

This equation is solved using the convolution integral, [38]:

$$\epsilon_s = \int_0^t \exp\left(-\frac{t-s}{\kappa}\right)\frac{d\epsilon}{ds}\, ds \; , \tag{35}$$

which, accounting for an incremental form between the configurations of time t_n and t_{n+1}, reads:

$$\epsilon_s = \exp\left(-\frac{\Delta t}{\kappa}\right)\epsilon_{sn} + \int_{t_n}^{t_{n+1}} \exp\left(-\frac{t-s}{\kappa}\right)\frac{d\epsilon}{ds}\, ds \; , \tag{36}$$

where the current time-step is typically approximated using the midpoint rule:

$$\epsilon_s = \exp\left(-\frac{\Delta t}{\kappa}\right)\epsilon_{sn} + \exp\left(-\frac{\Delta t}{2\kappa}\right)(\epsilon - \epsilon_n) \; . \tag{37}$$

Despite being trivial the above relations indicate a straightforward implementation of the quasi-nonlinear model contrary to a nonlinear ODE integration scheme.

3.2. 3D Quasi-Nonlinear Maxwell Element with Time Temperature Superposition

For a general 3D thermomechanical case, the total strain in a branch is the effective log-strain measure $\mathbf{E}_{\text{eff}} = \mathbf{E}_e - 3\alpha_\infty(T - T_0)\mathbf{I}$. In the i^{th} branch of the Generalized Maxwell Model, the internal log-strain-like variable is $\mathbf{\Gamma}_i$, its energetically conjugated co-rotational Kirchhoff stress $-\widehat{\boldsymbol{\tau}}_i$ and the strain in the spring $\mathfrak{E}_i = \mathbf{E}_e - 3\alpha_\infty(T - T_0)\mathbf{I} - \mathbf{\Gamma}_i$, giving the relation below for the elastic strain in a branch:

$$\mathfrak{E}_i = \mathbf{E}_{\text{eff}} - \mathbf{\Gamma}_i \; . \tag{38}$$

Separating into volumetric and deviatoric parts, Eq. (34) is restated as follows in terms of the tensor $\mathfrak{E}_i$:

$$\operatorname{tr}\dot{\mathfrak{E}}_{\mathrm{i}} + \frac{\operatorname{tr}\mathfrak{E}_i}{k_i} = \operatorname{tr}\dot{\mathbf{E}}_{\text{eff}} \; , \tag{39}$$

$$\operatorname{dev}\dot{\mathfrak{E}}_{\mathrm{i}} + \frac{\operatorname{dev}\mathfrak{E}_i}{g_i} = \operatorname{dev}\dot{\mathbf{E}}_e \; , \tag{40}$$

where $\operatorname{dev}\mathbf{E}_{\text{eff}} = \operatorname{dev}\mathbf{E}_e$ is used noting that thermal expansion is a purely volumetric contribution and, k_i and g_i are the bulk and shear time constants, positive for thermodynamical consistency as inferred from Eq. (32). These are related to the viscosity of the i^{th} dashpot as follows:

$$\eta_i = E_i\, e_i = K_i\, k_i = 2\, G_i g_i \; , \tag{41}$$

where, K_i and G_i are the branch bulk and shear moduli and are functions of the invariants of $\mathfrak{E}_i$, $\operatorname{tr}\mathfrak{E}_i$ and $\|\operatorname{dev}\mathfrak{E}_i\|^2$, respectively. In this study, $\|(\cdot)\|$ of a tensor is intended as its Frobenius norm, i.e., the square root of the double contraction with itself. These are expressed as $K_i = K_{i0}A_i(\operatorname{tr}\mathfrak{E}_i)$ and $G_i = G_{i0}B_i(\operatorname{tr}\mathfrak{E}_i, \|\operatorname{dev}\mathfrak{E}_i\|^2)$. K_{i0} and G_{i0} are the initial moduli at null strain and the expressions for the scaling variables, A_i and B_i, are as follows:

$$\begin{aligned} A_i &= f_{\text{reg}}(\operatorname{tr}\mathfrak{E}_i, \xi)\, A_{ti}(\operatorname{tr}\mathfrak{E}_i^2, V_{tj}) + C_{0i}(1 - f_{\text{reg}}(\operatorname{tr}\mathfrak{E}_i, \xi))\, A_{ci}(\operatorname{tr}\mathfrak{E}_i^2, V_{cj}) \; , \\ B_i &= f_{\text{reg}}(\operatorname{tr}\mathfrak{E}_i, \xi)\, B_{ti}(\|\operatorname{dev}\mathfrak{E}_i\|^2, D_{tj}) + C_{0i}(1 - f_{\text{reg}}(\operatorname{tr}\mathfrak{E}_i, \xi))\, B_{ci}(\|\operatorname{dev}\mathfrak{E}_i\|^2, D_{cj}) \; , \end{aligned} \tag{42}$$

where $f_{\text{reg}}(\operatorname{tr}\mathfrak{E}_i, \xi)$ is the logistic function, i.e., $f_{\text{reg}} = \frac{1}{1+e^{-\xi \operatorname{tr}\mathfrak{E}_i}} \in (0, 1)$, which along with its complement $(1 - f_{\text{reg}})$, provides additional scaling in compression, i.e., $\operatorname{tr}\mathfrak{E}_i < 0$ and $C_{0i} > 1$, for higher stiffness and vice versa; the regularisation constant ξ in the logistic function controls the width of the logistic sigmoid and can be adjusted to provide continuous and continuously differentiable functions for A_i and B_i. This form of regularisation allows the modelling of tension-compression asymmetry in the elastic regime. Furthermore, through the logistic function, the terms A_{ti} and B_{ti} are active in tension and, A_{ci} and B_{ci} in compression.

The explicit expression for A_{ti} is stated below:

$$A_{ti} \;\; = \;\; \frac{1}{\sqrt{V_{t1}\operatorname{tr}\mathfrak{E}_i^2 + V_{t2}}} + V_{t3}\left(V_{t4} + \tanh\left(V_{t5}\operatorname{tr}\mathfrak{E}_i^2\right)\right) \; , \tag{43}$$

which despite its complexity is intended to induce a sigmoid-like shape to the stress. Specifically, the first term on the RHS multiplied with $\mathrm{tr}\,\mathfrak{E}_i$, i.e., $\frac{1}{\sqrt{V_{t1}\,\mathrm{tr}\,\mathfrak{E}_i^2+V_{t2}}}\mathrm{tr}\,\mathfrak{E}_i$ is an algebraic sigmoid inducing such a shape at lower strains, and the second term $V_{t3}\left(V_{t4}+\tanh\left(V_{t5}\,\mathrm{tr}\,\mathfrak{E}_i^2\right)\right)$ is designed to scale the stress at higher strains. However, the constants $V_{tj=1,2,3,4,5}$ need not all be non-null, and their calibration largely depends on the material to be modelled which is outlined in Section 5.2. For A_{ci}, V_{tj} are replaced by V_{cj} and, for B_{ti} and B_{ci}, $\mathrm{tr}\,\mathfrak{E}_i^2$ by $\|\mathrm{dev}\,\mathfrak{E}_i\|$, V_{tj} by D_{tj} and D_{cj} respectively:

$$\begin{aligned}
A_{ci} &= \frac{1}{\sqrt{V_{c1}\,\mathrm{tr}\,\mathfrak{E}_i^2+V_{c2}}}+V_{c3}\left(V_{c4}+\tanh\left(V_{c5}\,\mathrm{tr}\,\mathfrak{E}_i^2\right)\right)\ ,\\
B_{ti} &= \frac{1}{\sqrt{D_{t1}\,\|\mathrm{dev}\,\mathfrak{E}_i\|^2+D_{t2}}}+D_{t3}\left(D_{t4}+\tanh\left(D_{t5}\,\|\mathrm{dev}\,\mathfrak{E}_i\|^2\right)\right)\ ,\\
B_{ci} &= \frac{1}{\sqrt{D_{c1}\,\|\mathrm{dev}\,\mathfrak{E}_i\|^2+D_{c2}}}+D_{c3}\left(D_{c4}+\tanh\left(D_{c5}\,\|\mathrm{dev}\,\mathfrak{E}_i\|^2\right)\right)\ .
\end{aligned} \tag{44}$$

The parameters V_{tj}, V_{cj}, D_{tj} and D_{cj} are material constants[1], which for numerical stability are posed to be either null or positive.

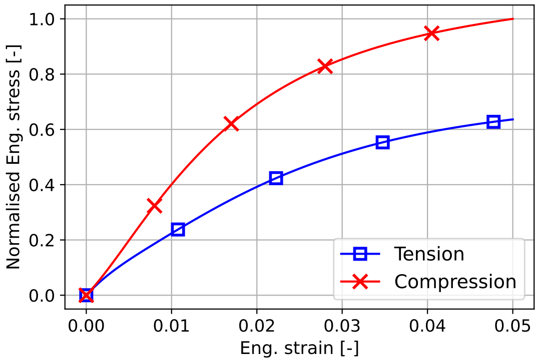

Figure 4: Tension-compression elastic asymmetry at low strains - Normalised engineering stress with increasing uniaxial strain.

The conjugated stress measure $\widehat{\boldsymbol{\tau}}_i$ is expressed in terms of the pressure ($\widehat{p}_i$) and deviator ($\mathrm{dev}\,\widehat{\boldsymbol{\tau}}_i$):

$$\widehat{p}_i = K_{i0}\,A_i(\mathrm{tr}\,\mathfrak{E}_i)\,\mathrm{tr}\,\mathfrak{E}_i\ , \tag{45}$$

$$\mathrm{dev}\,\widehat{\boldsymbol{\tau}}_i = 2G_{i0}\,B_i(\mathrm{tr}\,\mathfrak{E}_i, \|\mathrm{dev}\,\mathfrak{E}_i\|^2)\,\mathrm{dev}\,\mathfrak{E}_i\ . \tag{46}$$

The variation of this stress measure, and by extension of A_i and B_i in Eqs. (42), with uniaxial strain at low deformations is shown in Fig. 4 for a tension-to-compression modulus ratio of 0.6. The free energy contribution of each branch, $\widehat{\psi}_i$, is approximated to be regularised similarly, which for brevity is mentioned in Appendix A.1.

---

[1] V_{tj}, V_{cj}, D_{tj} and D_{cj} are written without the subscript 'i' for brevity but it is implied that every branch in the Quasi-nonlinear Maxwell model has unique V and D parameters.

3.3. Convolution integrals in shifted laboratory time

The convolution integrals akin to Eq. (35) are now performed in shifted laboratory time, i.e., material time. This allows the inclusion of the temperature dependency of relaxation phenomena while using the aforementioned temperature-independent material parameters. The relaxation time constants decrease with temperature, in an inverted Arrhenius rate form. In this sense, the exponential term in the Arrhenius rate equation will be positive [46]. Similarly, a parallel can be drawn using a suitable shift factor [47]. Stress relaxation is therefore said to occur in material time ($t^{\#}$) defined as:

$$\int_{s^{\#}}^{t^{\#}} d\upsilon^{\#} = \int_{s}^{t} \frac{d\upsilon}{a_T(\upsilon)} \,, \tag{47}$$

where υ is a dummy variable and $a_T(T)$ is the shift factor that describes the equivalence of higher strain rate to loading at a base strain rate but at a lower temperature [48], the so-called Time-Temperature equivalence. This reduced time is approximated numerically using Gaussian Quadrature, see Appendix A.2. The Williams-Landel-Ferry shift factor, a_T, is adopted here [49]:

$$a_T = \exp\left(-\frac{C_1(T - T_{\text{ref}})}{C_2 + T - T_{\text{ref}}}\right) \,, \tag{48}$$

where C_1 and C_2 are material constants and T_{ref} is the chosen reference temperature (typically the glass transition temperature). The above integral can be solved numerically to evaluate a shifted arbitrary time-step, i.e., time increment $\Delta t^{n^{\#}} = f(t^n - t^{n-1})$, for an arbitrary functional f [50]. Notice however that for a given functional being approximated through Gaussian Quadrature, the sampling points are different for the recursive and mid-step exponential terms in a solution such as Eq. (37), refer to Appendix A.2 for the formulation. Making this distinction, the solution to the ODEs Eqs. (39) and (40) in material time is as follows:

$$\begin{aligned}
\operatorname{tr}\mathfrak{E}_i &= \exp\left(-\frac{\Delta t^{\#}|_{\text{rec}}}{k_i}\right)\operatorname{tr}\mathfrak{E}_i^n + \exp\left(-\frac{\Delta t^{\#}|_{\text{mid}}}{k_i}\right)\left(\operatorname{tr}\mathbf{E}_{\text{eff}} - \operatorname{tr}\mathbf{E}_{\text{eff}}^n\right) \,, && (49)\\
\operatorname{dev}\mathfrak{E}_i &= \exp\left(-\frac{\Delta t^{\#}|_{\text{rec}}}{g_i}\right)\operatorname{dev}\mathfrak{E}_i^n + \exp\left(-\frac{\Delta t^{\#}|_{\text{mid}}}{g_i}\right)\left(\operatorname{dev}\mathbf{E}_e - \operatorname{dev}\mathbf{E}_e^n\right) \,, && (50)
\end{aligned}$$

where the time constants along with the initial moduli, K_{i0} and G_{i0}, in Eqs. (45) and (46) are identified from relaxation spectrum experiments. However, a dynamic Young's modulus is typically obtained from such experiments [51] and estimating a dynamic Poisson's ratio is complicated when tension-compression asymmetry is expected requiring extensive experimentation [52]. Therefore, the Poisson's ratio is assumed to be the same in all branches and the dynamic Young's modulus is obtained experimentally, making E_{i0} and e_i the parameters to be calibrated from relaxation spectrum experiments, following Eqs. (41), and a Poisson's ratio (the initial values as the moduli evolve with strain) to be assumed as suited.

3.4. Modification for Coaxial Stress

The approximation of convolution integral is written in non-constant intermediate configurations, i.e., the recursive addition in the solution to the convolution integrals in Eq. (50), contains the terms $\operatorname{dev}\mathfrak{E}_i^n$ and $\operatorname{dev}\mathbf{E}_e^n$ which exist in the co-rotational configuration of the previous time-step, see Fig. 3a. This addition of terms in different configurations leads to a loss of coaxiality as the deviatoric strain in the branch spring, $\operatorname{dev}\mathfrak{E}_i$, is not coaxial with the Hencky strain tensor, $\mathbf{E}_e$, or equivalently $\mathbf{E}_{\text{eff}}$ noting that volumetric expansion is frame invariant. Consequently, the deviatoric stress in Eq. (46), $\operatorname{dev}\widehat{\boldsymbol{\tau}}_i$, is not coaxial with the deviatoric strain in the branch spring, $\operatorname{dev}\mathfrak{E}_i$. This coaxiality is necessary to keep the Mandel stress, $\widehat{\mathbf{M}}_e$, symmetric for an isotropic material subjected to elastoplasticity [45]. The relation for $\operatorname{dev}\mathfrak{E}_i$ is subsequently modified using a rotation tensor, $\mathbf{R}$, intended to rotate the bases of a tensor existing in the co-rotational configuration at the previous time-step to the current one. Note that a tensor and its deviator have the same orthonormal bases. A convenient way of constructing such a rotation tensor is to form an orthonormal basis using the eigenvectors of the Hencky strain at the previous and current time-steps, i.e., $\mathbf{E}_e^n$ and $\mathbf{E}_e$. These tensors are expressed below in the spectral representation,

$$\mathbf{E}_e^n = \sum_{k=1}^{3} \omega_k^n \boldsymbol{N}_k^n \otimes \boldsymbol{N}_k^n \ , \tag{51}$$

$$\mathbf{E}_e = \sum_{k=1}^{3} \omega_k \boldsymbol{N}_k \otimes \boldsymbol{N}_k \ , \tag{52}$$

where ω_k are the eigenvalues and $\boldsymbol{N}_k$ the corresponding eigenvectors. Observing the above spectral representations, the rotated strain tensor from the previous time-step, $\mathbf{E}_e^{n*}$, is stated as follows:

$$\mathbf{E}_e^{n*} = \mathbf{R} \cdot \mathbf{E}_e^n \cdot \mathbf{R}^T = \sum_{k=1}^{3} \omega_k^n \boldsymbol{N}_k \otimes \boldsymbol{N}_k \ . \tag{53}$$

The following form of the rotation tensor, $\mathbf{R}$, can therefore be inferred,

$$\mathbf{R} = \sum_{k=1}^{3} \boldsymbol{N}_k \otimes \boldsymbol{N}_k^n \ , \tag{54}$$

which rotates tensors as shown in Fig. 3b. Lastly, Eq. (50) is modified as follows:

$$\operatorname{dev}\mathfrak{E}_i = \exp\left(-\frac{\Delta t^{\#}|_{\text{rec}}}{g_i}\right)\operatorname{dev}\mathfrak{E}_i^{n*} + \exp\left(-\frac{\Delta t^{\#}|_{\text{mid}}}{g_i}\right)\left(\operatorname{dev}\mathbf{E}_e - \operatorname{dev}\mathbf{E}_e^{n*}\right) \ , \tag{55}$$

where the same basis rotation is applied to $\mathfrak{E}_i^n$ which shares the same bases as $\mathbf{E}_e^n$ at a given time-step. Refer to Appendix A.3 for further details. Coaxiality is therefore enforced through the recursive addition of coaxial tensors.

3.5. Generalized Maxwell Model - Total Stress

The hyperelastic branch in the Generalized Maxwell Model is modelled in the same way as the other branches, except for the scaling variables, which are taken as the functions of the effective elastic strain, $\mathbf{E}_{\text{eff}}$, of which the pressure and deviatoric (via the logistic function) contributions of the purely hyperelastic branch are a function of:

$$\widehat{p}_{\infty} = K_{\infty 0} A_{\infty} \left(\operatorname{tr} \mathbf{E}_{\text{eff}}\right) \operatorname{tr} \mathbf{E}_{\text{eff}} \ , \tag{56}$$

$$\operatorname{dev} \widehat{\boldsymbol{\tau}}_{\infty} = 2 G_{\infty 0} B_{\infty} (\operatorname{tr} \mathbf{E}_{\text{eff}}, \|\operatorname{dev} \mathbf{E}_e\|^2) \operatorname{dev} \mathbf{E}_e \ , \tag{57}$$

where, the relations in Eqs. (43-44) are extended to the case of $i \to \infty$ to define $A_{t\infty}$, $A_{c\infty}$, $B_{t\infty}$ and $B_{c\infty}$, the moduli $K_{\infty 0}$ and $G_{\infty 0}$ are identified from relaxation spectrum experiments, and the parameters V_{tj}, V_{cj}, D_{tj} and D_{cj} are identified in a similar way as to their Maxwell branch counterparts. Finally, for the Generalized Maxwell Model with N branches, the thermoviscoelastic free energy contribution is written as:

$$\widehat{\psi}_{ve} = \widehat{\psi}_{\infty} + \sum_{i=1}^{N} \widehat{\psi}_i \ , \tag{58}$$

resulting in the final definition of the stress:

$$\widehat{\boldsymbol{\tau}}_e = \frac{\partial \widehat{\psi}_{\infty}}{\partial \mathbf{E}_e} + \sum_{i=1}^{N} \frac{\partial \widehat{\psi}_i}{\partial \mathfrak{E}_i} : \frac{\partial \mathfrak{E}_i}{\partial \mathbf{E}_e} = \left(\widehat{p}_{\infty} + \sum_{i=1}^{N} \widehat{p}_i \right) \mathbf{I} + \left(\operatorname{dev} \widehat{\boldsymbol{\tau}}_{\infty} + \sum_{i=1}^{N} \operatorname{dev} \widehat{\boldsymbol{\tau}}_i \right) \ , \tag{59}$$

where, through the relation $\mathfrak{E}_i = \mathbf{E}_{\text{eff}} - \boldsymbol{\Gamma}_i$, the derivative $\frac{\partial \mathfrak{E}_i}{\partial \mathbf{E}_e}$ stems from the convolution integral approximations in Eqs. (49) and (55), the closed form expression is explicitly mentioned in [53]. This methodology effectively represents the quasi-nonlinear Maxwell model shown in Fig. 2. The explicit expression $\widehat{\psi}_{\infty}$ is presented in Appendix A.1 for brevity. As for the thermoviscoelastic dissipation, $\hat{\delta}_{ve}$:

$$\hat{\delta}_{ve} = \sum_{i=1}^{N} \widehat{\boldsymbol{\tau}}_i : \frac{d}{dt} \left(\mathbf{E}_{\text{eff}} - \mathfrak{E}_i \right) \ . \tag{60}$$

4. Thermoviscoplasticity

The plastic driving stress from Eq. (16) is the Mandel stress, $\widehat{\mathbf{M}}_e$. Noting the conjugacy relation in the elastic power, $\frac{1}{2}\widehat{\mathbf{S}}_e : \dot{\mathbf{C}}_e = \widehat{\boldsymbol{\tau}}_e : \dot{\mathbf{E}}_e$, for coaxial $\widehat{\boldsymbol{\tau}}_e$ and $\mathbf{E}_e$, the Mandel stress is symmetric since commutativity ($\mathbf{C}_e \widehat{\mathbf{S}}_e = \widehat{\mathbf{S}}_e \mathbf{C}_e$) is ensured by coaxiality and it is equivalent to the co-rotational Kirchhoff stress, i.e., $\widehat{\mathbf{M}}_e = \widehat{\boldsymbol{\tau}}_e$ [2]. Because of this equivalence $\widehat{\boldsymbol{\tau}}_e$ is taken as the plastic driving stress and the rate of plastic deformation is consequently symmetric, i.e., $\mathbf{L}_p = \mathbf{D}_p$, which is expected for an isotropic material [45].

---

[2] Note that, $\widehat{\mathbf{S}}_e = \widehat{\boldsymbol{\tau}}_e : \frac{\partial \ln \mathbf{C}_e}{\partial \mathbf{C}_e} = \widehat{\boldsymbol{\tau}}_e : \left(\boldsymbol{\mathcal{I}}^{\,2.1} \mathbf{C}_e^{-1} \right) = \frac{1}{2} \left(\widehat{\boldsymbol{\tau}}_e \mathbf{C}_e^{-1} + \left(\widehat{\boldsymbol{\tau}}_e \mathbf{C}_e^{-1} \right)^T \right)$, with $\boldsymbol{\mathcal{I}}$ as the 4th order symmetric identity tensor. This leads to: $\widehat{\mathbf{M}}_e = \frac{1}{2} \left(\widehat{\boldsymbol{\tau}}_e + \mathbf{C}_e \widehat{\boldsymbol{\tau}}_e \mathbf{C}_e^{-1} \right) = \widehat{\boldsymbol{\tau}}_e$ since $\widehat{\boldsymbol{\tau}}_e$ permutes with $\mathbf{C}_e$.

4.1. Internal Variables and Dissipation Potential

The thermoviscoplastic free energy per unit reference volume is $\widehat{\psi}_{vp}\,(T,\boldsymbol{\alpha},r)$, referring to Eq. (15). The internal variables are conjugated to the backstress ($\mathbf{B}$) and the isotropic hardening force (R), respectively:

$$\mathbf{B} = \frac{\partial \widehat{\psi}_{vp}}{\partial \boldsymbol{\alpha}} \quad \text{and} \quad R = \frac{\partial \widehat{\psi}_{vp}}{\partial r} \ . \tag{61}$$

Mechanical dissipation corresponding to TVP of the CDI is restated below from Section 2.2:

$$\widehat{\delta}_{vp} = \widehat{\boldsymbol{\tau}}_e : \mathbf{D}_p - \mathbf{B} : \dot{\boldsymbol{\alpha}} - R\dot{r} \geq 0 \ , \tag{62}$$

which must be satisfied for thermodynamical consistency. The flow rule and evolution equations are derived from the viscoplastic dissipation potential, φ^*, typically expressed as:

$$\varphi^* \ = \ \Omega_p + \Omega_r \ , \tag{63}$$

$$\Omega_p \ = \ \Omega_p\left(\lambda P\left(I_1(\widehat{\boldsymbol{\tau}}_e - \mathbf{B}), J_2(\widehat{\boldsymbol{\tau}}_e - \mathbf{B})\right), R; T, \boldsymbol{\alpha}, r\right) \ , \tag{64}$$

$$\Omega_r \ = \ \Omega_r\left(\mathbf{B}, R; T, \boldsymbol{\alpha}, r\right) \ , \tag{65}$$

where Ω_p is the plastic part and Ω_r is the recovery part, P is the plastic potential, λ is the viscoplastic multiplier and, I_1, J_2 are the invariants of the effective stress tensor $\boldsymbol{\phi} = \widehat{\boldsymbol{\tau}}_e - \mathbf{B}$. The non-associative flow rule then becomes:

$$\mathbf{D}_p = \frac{\partial \varphi^*}{\partial \widehat{\boldsymbol{\tau}}_e} = \frac{\partial \Omega_p}{\partial \widehat{\boldsymbol{\tau}}_e} = \frac{\partial \Omega_p}{\partial P}\frac{\partial P}{\partial \widehat{\boldsymbol{\tau}}_e} = \lambda \frac{\partial P}{\partial \widehat{\boldsymbol{\tau}}_e} \ , \tag{66}$$

where $\frac{\partial P}{\partial \widehat{\boldsymbol{\tau}}_e}$ is the plastic flow direction and the viscoplastic multiplier λ is assumed to be of the following Perzyna form, [54]:

$$\lambda \ = \ \frac{1}{\eta(T)}\langle F \rangle^{\frac{1}{p}} \ , \tag{67}$$

where F is the yield function, $\eta(T)$ is the temperature-dependent viscosity coefficient, p is the rate-sensitivity parameter and $\langle\cdot\rangle$ are the Macaulay brackets. The temperature-dependency of viscosity is expressed in the form: $\eta(T) = \eta \ a_{T_\eta}(T)$, where η is a constant (although extension to internal variable dependency is straight-forward), and a_{T_η} is a shift factor-like negative exponential function [31]. The evolution equation for $\boldsymbol{\alpha}$ follows the property $\frac{\partial P}{\partial \mathbf{B}} = -\frac{\partial P}{\partial \widehat{\boldsymbol{\tau}}_e}$ through $\boldsymbol{\phi} = \widehat{\boldsymbol{\tau}}_e - \mathbf{B}$, and ignoring the recall term, $\frac{\partial \Omega_r}{\partial \mathbf{B}}$, to obtain the following:

$$\dot{\boldsymbol{\alpha}} = -\frac{\partial \varphi^*}{\partial \mathbf{B}} = -\frac{\partial \Omega_p}{\partial P}\frac{\partial P}{\partial \mathbf{B}} = -\lambda \frac{\partial P}{\partial \mathbf{B}} = \mathbf{D}_p \ . \tag{68}$$

The evolution equation for r is assumed to be:

$$\dot{r} = -\frac{\partial \varphi^*}{\partial R} = -\frac{\partial \Omega_p}{\partial R} - \frac{\partial \Omega_r}{\partial R} = \dot{\gamma} - \frac{\partial \Omega_r}{\partial R} \ , \tag{69}$$

where γ is the equivalent plastic strain. The term $\frac{\partial \Omega_r}{\partial R}$ is assumed to be 0 in this study, which makes $\dot{r} = \dot{\gamma}$. The equivalent plastic strain rate ($\dot{\gamma}$) is taken as:

$$\dot{\gamma} = k\sqrt{\mathbf{D}_p : \mathbf{D}_p}\ , \tag{70}$$

adopted from [55]. The parameter k is written in terms of the initial plastic Poisson's ratio, ν_p, as:

$$k = \frac{1}{\sqrt{1 + 2\nu_p^2}}\ . \tag{71}$$

For incompressible plastic flow $\nu_p = 0.5$ giving the classical value of $k = \sqrt{\frac{2}{3}}$ for purely deviatoric plasticity. Lastly, a suitable quadratic form of the plastic potential (P) is chosen to capture volumetric and deviatoric plastic flows:

$$P(\boldsymbol{\phi}) = \phi_e^2 + \beta\phi_p^2\ , \tag{72}$$

where the invariants of the effective stress tensor, $\boldsymbol{\phi}$, are:

$$\phi_e = \sqrt{\frac{3}{2}\,\mathrm{dev}\,\boldsymbol{\phi} : \mathrm{dev}\,\boldsymbol{\phi}} \quad \text{and} \quad \phi_p = \frac{1}{3}\mathrm{tr}\,\boldsymbol{\phi}\ , \tag{73}$$

and β is a constant material parameter related to the plastic Poisson's ratio at the onset of plastic flow as follows:

$$\nu_p = \frac{9 - 2\beta}{18 + 2\beta}\ . \tag{74}$$

This value is expected to decrease due to backstress but remains positive as was also the case in [22]. Consequently, the definition of the thermoviscoplastic free energy, $\widehat{\psi}_{vp}$, is taken as follows:

$$\widehat{\psi}_{vp} = \underbrace{\frac{1}{2}k^2 H_{\mathbf{B}}(\gamma, T)\ \boldsymbol{\alpha} : \boldsymbol{\alpha}}_{kinematic} + \underbrace{\int R(\gamma, T) d\gamma}_{isotropic}\ . \tag{75}$$

Therefore, the relationship between $\mathbf{B}$ and $\boldsymbol{\alpha}$ becomes:

$$\mathbf{B} = \frac{\partial \widehat{\psi}_{vp}}{\partial \boldsymbol{\alpha}} = k^2 H_{\mathbf{B}}(\gamma, T)\boldsymbol{\alpha}\ , \tag{76}$$

where $H_{\mathbf{B}}$ is the kinematic hardening modulus dependent on γ and T, this temperature dependency can be linearly separated such that $H_{\mathbf{B}}(\gamma, T) = a_{T_{\mathbf{B}}}(T)H_{\mathbf{B}}(\gamma)$ with $a_{T_{\mathbf{B}}}(T)$ being a shift factor-like function. In line with an additive isotropic hardening formulation, it is reasonable to assume:

$$R = \frac{\partial \widehat{\psi}_{vp}}{\partial \gamma} = a_{T_\gamma}(T)\,\sigma(\gamma)\ , \tag{77}$$

where $\sigma(\gamma)$ is the yield stress-like non-linear function of γ to be established later and $a_{T_\gamma}(T)$ is again a shift factor-like function to describe the temperature dependency of the yield stress. Using the relation Eq. (68) and the definitions in Eqs. (76) and (77), the mechanical dissipation is written as:

$$\widehat{\delta}_{vp} = (\widehat{\boldsymbol{\tau}}_e - \mathbf{B}) : \mathbf{D}_p - R\dot{\gamma} \geq 0 \ . \tag{78}$$

In the following, unless stated otherwise, for brevity, the viscosity and the hardening moduli are written assuming that the temperature dependency lies within, i.e., η and $H_{\mathbf{B}}$ are presumed to be $\eta(\gamma, T)$ and $H_{\mathbf{B}}(\gamma, T)$, respectively.

4.2. Kinematic Hardening Evolution

The rate equation for $\mathbf{B}$ is written using Eq. (76) in terms of T, γ and $\boldsymbol{\alpha}$, and using the rate form of $\boldsymbol{\alpha}$ in Eq. (68):

$$\dot{\mathbf{B}} = k^2 H_{\mathbf{B}} \mathbf{D}_p + \frac{1}{H_{\mathbf{B}}} \frac{\partial H_{\mathbf{B}}}{\partial \gamma} \dot{\gamma} \mathbf{B} + \frac{1}{H_{\mathbf{B}}} \frac{\partial H_{\mathbf{B}}}{\partial T} \dot{T} \mathbf{B} \ , \tag{79}$$

which is similar to that of [44] with the static recovery terms ignored. The 2^{nd} term on the RHS is the dynamic recall term and the term with temperature rate improves the performance under rapid temperature changes [44]. Lastly, $H_{\mathbf{B}}$ is taken as a polynomial expression in terms of the equivalent plastic strain (γ):

$$H_{\mathbf{B}} = a_{T_{\mathbf{B}}} \sum_{k=1}^{N_k} h_{k-1} \gamma^{k-1} \ , \tag{80}$$

where k is the order of the polynomial, h_{k-1} are material constants, and the dependencies on temperature and equivalent plastic strain are explicitly stated.

4.3. Isotropic Hardening Force

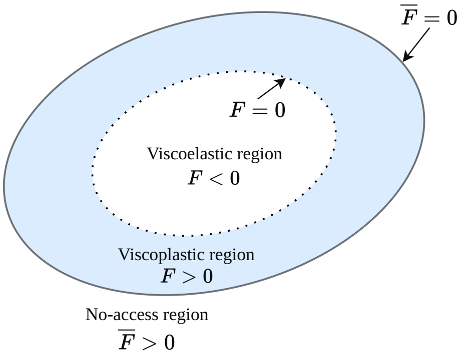

Figure 5: Extended power-yield surface [22]

The definition of R is linked to the yield function. To capture pressure dependent yielding, the Drucker-Prager-like power yield function, F, introduced in [22], is adopted:

$$F(\Delta\gamma, T) = a_2 \phi_e^{\alpha} - a_1 \phi_p - a_0 \ , \tag{81}$$

where α is the power yield model parameter (not to be confused either with $\boldsymbol{\alpha}$, the backstrain, or with α_∞, the coefficient of thermal expansion). The coefficients, a_2, a_1 and a_0, are derived from uniaxial compressive and tensile yielding conditions (although general loading cases are sufficient to furnish two distinct pressure states as noted in [22]), which leads to:

$$a_2 = \frac{1}{\sigma_c^\alpha} \ , \quad a_1 = 3\frac{m^\alpha - 1}{m+1}\frac{1}{\sigma_c} \ , \quad \text{and} \quad a_0 = \frac{m^\alpha + m}{m+1} \ . \tag{82}$$

Then, the ratio of yield stresses in tension and compression, m, and the rate of the yield stresses, respectively, are written as:

$$m = \frac{\sigma_t}{\sigma_c} \quad \text{and} \quad \dot{\sigma}_{t|c}\big|_T = a_{T_{\gamma\,t|c}}(T)\, H_{t|c}(\gamma)\,\dot{\gamma} \ , \tag{83}$$

where $a_{T_{\gamma\,t|c}}$ are the temperature functions and $H_{t|c}$ are the hardening moduli in tension or compression, respectively. The adopted yield function was shown to be convex for all values of the equivalent plastic strain as long as the power yield parameter satisfies $\alpha \geq 1$ [22]. In the viscoplastic range, using the viscoplastic consistency parameter, λ, and Eq. (81), the extended yield condition, $\bar{F}$, see Fig. 5, is defined as:

$$\bar{F}(\lambda, \Delta\gamma, T) = a_2 \phi_{\boldsymbol{e}}^\alpha - a_1 \phi_p - a_0 - (\eta\lambda)^p \ . \tag{84}$$

Also, the viscosity is expressed as:

$$\eta = a_{T_\eta}(T)\,\eta_0 \ , \tag{85}$$

where a_{T_η} is a temperature function and η_0 is the constant value of viscosity at the reference temperature. As the integrated form of the rate equation in Eq. (83) is desirable, the following relations for the tensile and compressive yield stresses are adopted:

$$\sigma_{t|c} = a_{T_{\gamma\,t|c}}(T)\ \left[\sigma_{t_0|c_0} + h_{t_0|c_0}\gamma + h_{t_1|c_1}\left(1 - \exp(-h_{t_2|c_2}\gamma)\right)\right] \ , \tag{86}$$

where the relations are linear exponential in terms of γ, and $\sigma_{t_0|c_0}$ are the initial tensile and compressive yield stresses, respectively, i.e., at the onset of plasticity. Then, ${h_k}^{c|t}$ are material constants to be calibrated later. Following the developments of [31], the following form of isotropic hardening force, R, is assumed depending only on the compressive yield stress:

$$R = \sigma_c - {a_{T_\gamma}}^c(T)\,\sigma_{c_0} \ , \tag{87}$$

which is similar in form to Eq. (77) with the explicit temperature dependency and nonlinear functions of the equivalent plastic strain within the yield stress.

4.4. *Summary of the Constitutive Model*

The workflow of the model in the current time interval of $[t^n, t^{n+1}]$, with the current time-step $\Delta t = t^{n+1} - t^n$, is the (visco)elasto-(visco)plastic integration algorithm, detailed in Appendix B. In a kinematically based FEM, the independent variables for the current time-step, namely, $\{\mathbf{F}, T, \boldsymbol{H}\}$ are available from the finite element Newton-Raphson resolution which, following elastic predictions and plasticity corrections, are subsequently used to determine the dependent quantities. Since the interest is in obtaining the 1^{st} Piola-Kirchhoff stress in the undamaged state, $\widehat{\mathbf{P}}$, the 2^{nd} Piola-Kirchhoff stress in the intermediate configuration, $\widehat{\mathbf{S}}_e$ obtained from $\hat{\boldsymbol{\tau}}_e$, is used as follows :

$$\widehat{\mathbf{P}} = \mathbf{F}_e \cdot \widehat{\mathbf{S}}_e \cdot \mathbf{F}_p^{-1} \, . \tag{88}$$

In the (pseudo-)damaged state, this is modified as:

$$\mathbf{P} = \zeta(\widehat{\psi}, \widehat{\psi}_{\max})\widehat{\mathbf{P}} \, , \tag{89}$$

using the definition of ζ in Eq. (24). The free energy in the undamaged state is given by Eq. (15), refer to Appendix A.1 for the explicit expressions in thermoviscoelasticity, and $\widehat{\psi}_{\max}$ is as described previously in Eq. (7). The heat flux in the reference configuration, $\boldsymbol{Q}$, is given by Eq. (14). As for the heat source, the viscoelastic dissipation and the Gough-Joule terms are ignored for simplicity, and C_d is taken to be equivalent to C_p, the specific heat at constant hydrostatic pressure following the discussion in [31]. The mechanical heat source, W_M, in the (pseudo-)damaged state is restated by modifying the terms in Eq. (29) using the plastic power in terms of $\boldsymbol{\phi}$ using Eq. (78), the definition of specific heat and ignoring the external heat source term (following a lack of intention of applying such a boundary condition),

$$W_M = \zeta \left(-C_p \dot{T} + \boldsymbol{\phi} : \mathbf{D}_p - R\dot{\gamma} \right) - \frac{\partial \psi}{\partial \widehat{\psi}_{\max}} \dot{\widehat{\psi}}_{\max} \, . \tag{90}$$

A further assumption is made to ignore the $R\dot{\gamma}$ term in the above equation to allow the plastic power to contribute fully to heat dissipation, but is left in the formulation. To fully complete the problem the tangent operators are derived and reported in Appendix C.

5. Experimentation and Characterisation

The calibration of the constitutive model is split into experimentation and identification. The parameters noted before in Sections 3 and 4 are summarised in Table 1 including the necessary experimental tests. Therefore, a suitable experimental campaign consists of Dynamic Mechanical Analyses to calibrate the thermoviscoelastic relaxation spectrum and Williams-Landel-Ferry shift factor constants; uniaxial monotonic tension and compression tests at different strain rates and temperatures to identify the parameters of quasi-nonlinear thermoviscoelasticity, yield exponent and viscosity parameters, and hardening laws in thermoviscoplasticity; lastly, uniaxial cyclic loading test in tension and/or compression to calibrate Mullins' effect parameters. For the thermal properties, however, values are taken from the literature unless mentioned otherwise.

5.1. Experimental Campaign

The choice of semi-crystalline polymers is made considering sufficient stiffness over a wide range of temperatures spanning glass transition, traceable sensitivity to strain rates, reversible glass transition with a tractable transition range and sufficiently high melting point. Therefore, choosing a co-polymer BJ380MO Polypropylene (PP) grade from Borealis GmbH [56] and elastomeric Thermoplastic Polyurethane (TPU) grade EOS TPU 1301 from EOS GmbH [57] are deemed pertinent.

5.1.1. Polypropylene BJ380MO

ISO 527-1A material samples are injection moulded following the processing recommendations of the material supplier's datasheet [56] and the ISO standard, with a DEMAG IntElect 100/470-340 horizontal injection moulding machine, see Fig. 6a and Fig. 6b for the dimensions. Tool and mass temperatures are set at 45 and 230 ºC, respectively. A double cavity is filled at 1.4 s injection time and 285 bar filling pressure, followed by a 15 s long packing phase under 230 bar pressure. All dynamical mechanical analyses are carried out on the Metravib +300 DMA in tension mode using 20mm trimmed rectangular samples from the gauge section of the ISO 527-1A samples. At constant static displacement (5×10^{-5}m) and frequency (10 Hz) conditions, firstly, the linear viscoelastic region of the material is determined by performing a dynamic amplitude sweep from 1×10^{-6} to 10^{-5} m at constant temperature (23 ºC); secondly, to determine the glass transition range, at constant dynamic amplitude (5×10^{-6}m), a temperature sweep from -30 to 150°C is performed to observe the fluctuations in the loss factor ($\tan \delta$) and reduction in the storage modulus, see Figs. 7. From Fig. 7a, a loss of linearity is observed at a dynamic amplitude of 6×10^{-6}m; a transition range between -8 to 35 °C is inferred from Fig. 7b.

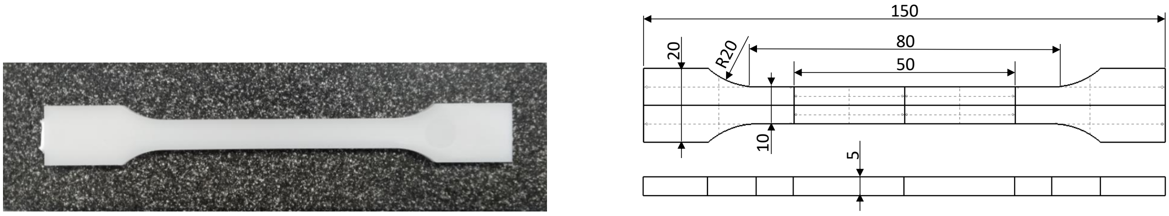

(a) Injection molded coupons.

(b) ISO 527-1A geometry and dimensions (in mms).

Figure 6: ISO 527-1A Polypropylene BJ380MO Samples.

To calibrate the TVE relaxation spectrum and shift factor a master curve is constructed through horizontally shifted frequency sweep isotherms. This requires a broad range of frequencies and

Table 1: Material parameters and Identification.

Group	Description	Notation	Identification Tests
Thermoviscoelasticity	Relaxation Spectrum	E_i, e_i (Eqs. 41)	Dynamic Mechanical Analysis (DMA) frequency sweeps in the relevant temperature range.
	WLF Shift factor constants	C_1, C_2 (Eq. 48)	
	Glass transition temperature	T_g/T_{ref} (Eq. 48)	One DMA dynamic amplitude sweep.
	Poisson's ratio	ν (Section 3.2)	*Literature*
	Quasi-nonlinear TVE parameters	V_{tj}, V_{cj}, D_{tj}, D_{cj}, C_j (Section 3.2)	Uniaxial tension and compression tests at fixed strain rate and temperatures.
Thermoviscoplasticity	Yield exponent	α (Eq. 84)	Monotonic uniaxial tests with varying degrees of stress triaxiality.
	Plastic Poisson's ratio	ν_p (Eq. 74)	One uniaxial monotonic test at fixed strain rate and reference temperature.
	Viscosity parameters	η, p	Monotonic uniaxial tests at different strain rates and temperatures.
	Viscosity temperature function	a_{T_η} (Eq. 85)	
	Hardening Laws	σ_c, σ_t, $H_{\mathbf{B}}$ (Eqs. 86)	Monotonic uniaxial tests at different strain rates and temperatures.
	Hardening temperature functions	${a_{T_\gamma}}^c$, ${a_{T_\gamma}}^t$, $a_{T_{\mathbf{B}}}$ (Eqs. 86)	
Mullins' effect	Mullins' parameter	z (Eq. 24)	Cyclic uniaxial tests at different temperatures.
	Mullins' parameter temperature function	a_{T_ζ} (Eq. 2.2)	
Thermal parameters at room temperature	Coefficient of Thermal Expansion	α_∞ (Eq. 3.2)	Thermomechanical Analysis (TMA)
	Specific heat	C_p (Eq. 90)	Differential Scaling Calorimetry (DSC)
	Coefficient of thermal conductivity	χ (Eq. 14)	Thermal Dilatometry

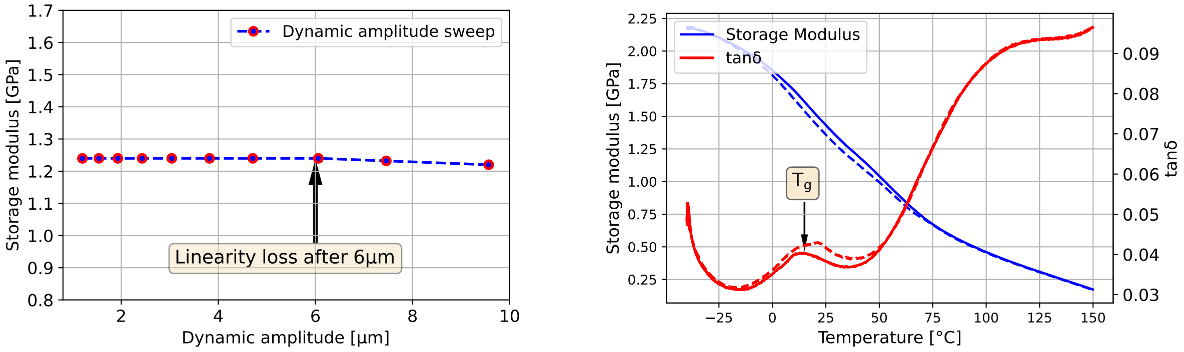

(a) Linear Viscoelastic Region

(b) Glass Transition Region

Figure 7: Preliminary DMA Results - Polypropylene BJ380MO

sufficient temperature steps to produce a good overlap in the shifted curves. Following this, at constant static displacement (5×10^{-5}m) and dynamic amplitude (5×10^{-6}m), on samples with a gauge length of 20 mm trimmed from the ISO 527-1A samples, frequency sweeps are performed in a range of 0.1 to 100 Hz at constant temperatures in a range of -10 to -70 °C with +10 °C increments, see Figs. 8a and 8b. Uniaxial monotonic tension and compression tests are performed on MTS Insight universal testing machine, at -10, 23 and 70 °C and low strain rate. These 3

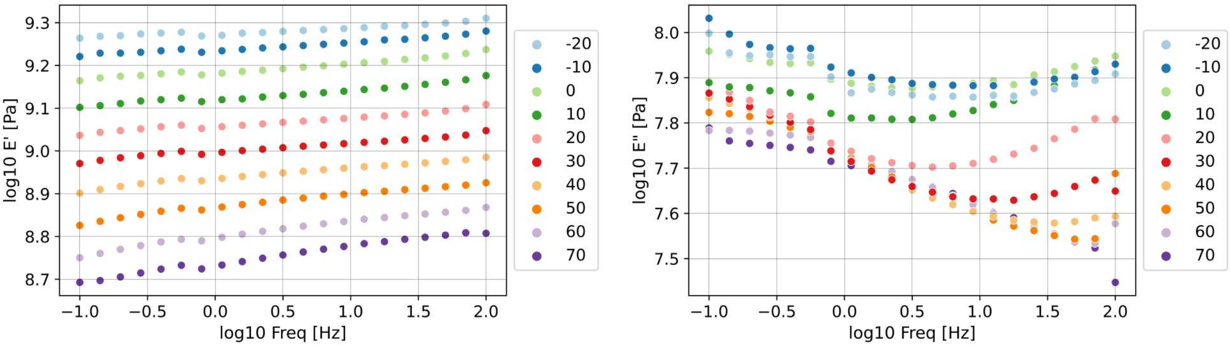

(a) Storage Modulus

(b) Loss Modulus

Figure 8: Modulus Isotherms from DMA - Polypropylene BJ380MO

temperatures are in the glassy, transition and rubbery regions respectively, and are achieved by placing the specimens in the temperature chamber Dycometal CETM -70/74e, 2 hours for 70°C and 24 hours for -10°C. Uniaxial tensile tests are also conducted on MTS High Rate System with strain rates of 0.5 and 5.0s^{-1} at 23°C. Uniaxial cyclic tests in tension are carried out using the same equipment at the three temperatures, -10, 23 and 70°C, where loading is performed at a low strain rate up to a specified strain value at each cycle followed by sudden unloading until zero strain. Before applying a subsequent load-unload cycle, a 300s dwell time is allowed. The strains are measured using the MTS mechanical extensometer and GOM Aramis camera system in the aforementioned cases. Lastly, thermomechanical analysis (TMA) for thermal dilatation coefficient is conducted on Weisstechnik LabEvent L C/100/40/5 temperature chamber with GOM camera system to measure the thermal strain and Differential Scaling Calorimetry (DSC) for specific heat on TA Q100 DSC. The thermal dilatation coefficient and specific heat per unit volume are found to be $6. \times 10^{-5}$K^{-1} and 1.7195×10^{6}J K^{-1}m^{-3}, respectively. The thermal conductivity is assumed to be 0.14Wm^{-1}K^{-1}, a nominal value for low-density thermoplastics. These values are summarised in Table D.7 in Appendix D.

5.1.2. Thermoplastic Polyurethane EOS 1301

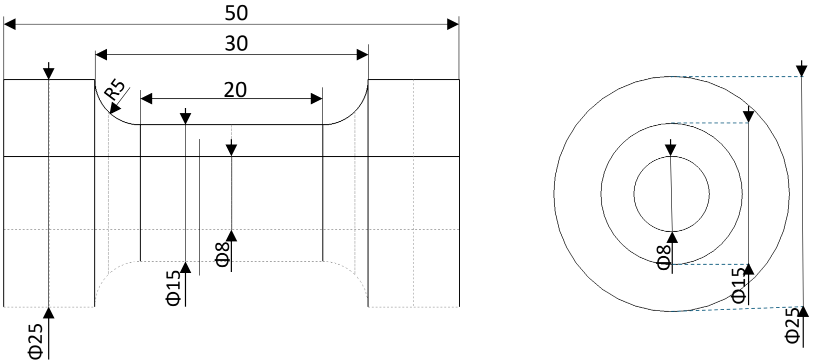

Figure 9: Dimensions (in mm) of SLS-printed hollow dumbbell specimens [58].

The experimentation for TPU is performed using additively manufactured (Selective Laser

Sintering) specimens that differ in their composition owing to different angles of printing, details of which are found in [58] and [59]. Uniaxial monotonic and cyclic experimental data are treated as bulk isotropic material behaviour by restricting to tests representing the full deformation range irrespective of differences in sample production due to additive manufacturing. In the case of DMA, frequency sweeps are performed in a range of 1 to 30 Hz at constant temperatures in a range of -130 to 120°C with +10°C increments with a heating rate of 2°C/min and an amplitude of 20µm on Q800 TA Instruments using SLS-printed single cantilever samples of dimensions 30 × 10 × 3 mm, refer to [59] for data and sample information. Uniaxial monotonic and cyclic tensile tests are performed on universal testing machine INSTRON 5966 with a 2kN loadcell at room temperature using SLS printed dogbone samples (ISO 527) and compression tests on INSTRON 5966 with a 10kN loadcell at room temperature using SLS printed rectangular samples of dimensions $15 \times 15 \times 30$ mm. In the cyclic tensile tests, samples are loaded until the extension is 9mm more than the step before and unloaded until a force of 0N. In contrast, in the cyclic compression tests, samples are loaded until the extension is -1mm more than the step before and unloaded to a force of -1N. The details of the samples are provided in [59]. The glass transition temperature here is inferred to be -30°C from the data provided by [59]. Additionally, the average value of the thermal dilatation coefficient assumed from [60], the specific heat per unit volume –for which density of laser sintered TPU is taken from [61] and assumed specific heat capacity from [60]– and the thermal conductivity assumed from [62] are respectively $1.5 \times 10^{-4}\mathrm{K}^{-1}$, $2.0535 \times 10^{6} J\mathrm{K}^{-1}\mathrm{m}^{-3}$ and $0.2332\mathrm{Wm}^{-1}\mathrm{K}^{-1}$, as summarised in Table D.11 in Appendix D.

Furthermore, for validation of the QNL model and the subsequent coaxial modifications, torsion tests are performed on SLS-printed hollow dumbbell specimens, dimensions reported in Fig. 9, on a ZwickRoell LTM10 Linear testing system with a cell of nominal torque 100Nm. The twist is applied on the curved outer surface of the upper bell while the curved outer surface of the lower bell is held by the machine grips in Fig. 10a. Two types of constraints are considered, one with no axial displacement constraint on the top-most surface of the upper bell to predict a positive Poynting effect [63] and second with the constraint to predict the resulting axial force. The shape induced due to torsional instability is shown in Fig. 10b.

5.2. Parameter Identification

Identification is split into two sections, which discuss the general methodology behind constructing the master curve using DMA frequency sweeps, followed by the specialisation of certain aspects of the constitutive model for each material introduced before.

5.2.1. Relaxation Spectrum and Shift Factor

The master curve is representative of the Time-Temperature Superposition principle, hence, high temperatures correspond to high times and low moduli, and vice versa. Therefore, the data

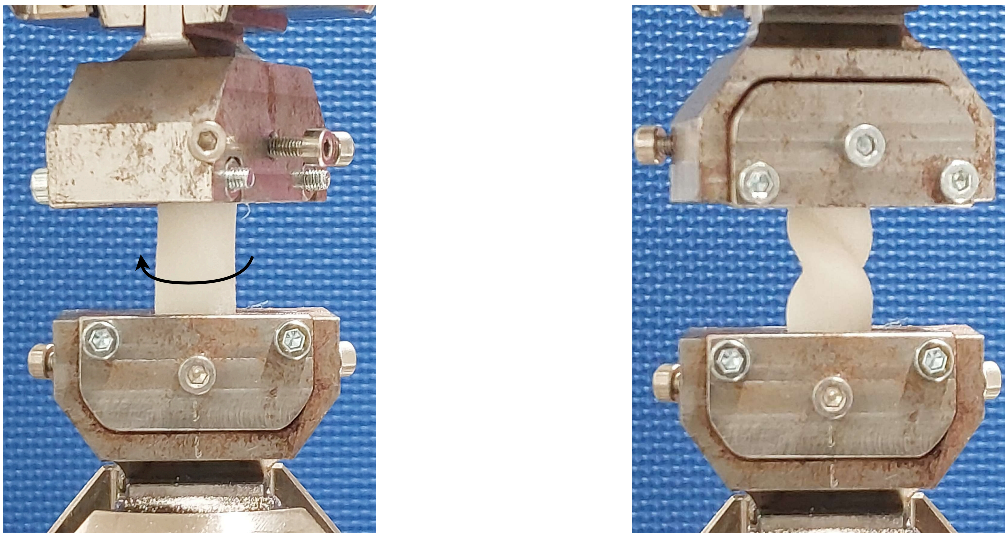

(a) Direction of twist is annotated. Image taken after a few degrees of twist. (b) Shape induced by torsion instability after large degrees of twist.

Figure 10: Experimental setup and deformation evolution for torsion tests on the SLS-printed hollow dumbbell specimens [59].

obtained from the frequency sweeps is shifted horizontally in a storage/loss modulus versus frequency plot in a log-log scale [64, 51]. The choice of storage ($E^{'}(t)$) or loss ($E^{''}(t)$) moduli depends on the quality of overlap and monotonicity across temperature steps. Noting the high degree of non-monotonicity associated with the loss modulus in the case of polypropylene, see Fig. 8b, the dynamic modulus data is used to make the master curve, where, $E = \sqrt{E'^{2} + E''^{2}}$. The dynamic modulus master curve is constructed using the concepts of overlap window and intermediate interpolation adopted from [64]. The reference temperatures are assumed to be 20 and -30°C for polypropylene and TPU, respectively. The master curves constructed for polypropylene and TPU are shown in Figs. 11a and 11b, which are modified to fit the slopes found in uniaxial tensile experiments and are elaborated in the following subsection 5.2.2. The horizontal shifts at a corresponding temperature used in the master curves are curve-fit to the empirical shift factor relation, Eq.(48), using the scipy optimisation module [65]. These curve-fits along with the WLF constants for each material are shown in Figs. 12.

An optimisation problem is then defined to obtain the $(2N + 1)$ parameters of the relaxation spectrum, where N corresponds to the number of Maxwell branches. The dynamic modulus master curves are the observed data. The “shifted” time range (reciprocal of shifted frequency) obtained through the horizontal shifts is used to generate the predicted data of dynamic modulus following the Prony series relation:

$$E(t) = E_{\infty} + \sum_{i=1}^{N} E_i \exp\left(-\frac{t}{e_i}\right) , \tag{91}$$

where, pertaining to the Generalized Maxwell model (quasi-nonlinear or otherwise), E_{∞} is the modulus of the infinite branch, E_i are the branch spring moduli and e_i are the time constants.

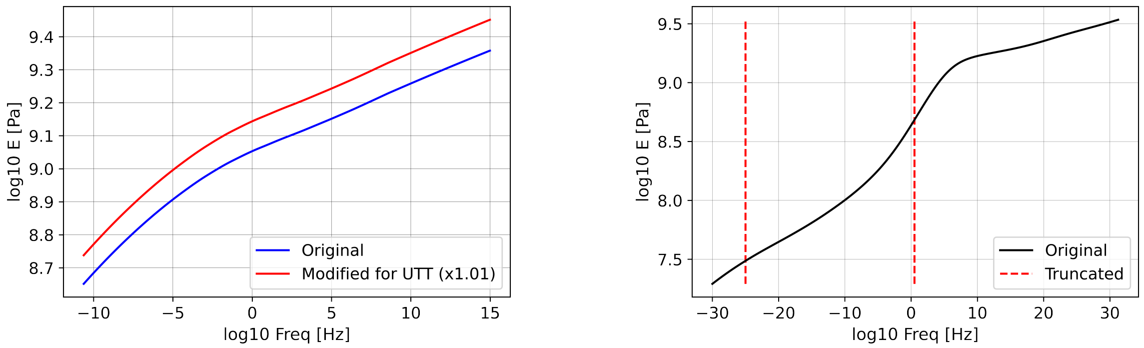

(a) PP BJ380MO - Constructed and modified to fit the data from UTT experiments.

(b) TPU EOS 1301 - Constructed and truncated to fit the data from UTT experiments.

Figure 11: Master curves of dynamic modulus vs frequency in log10-log10 plots.

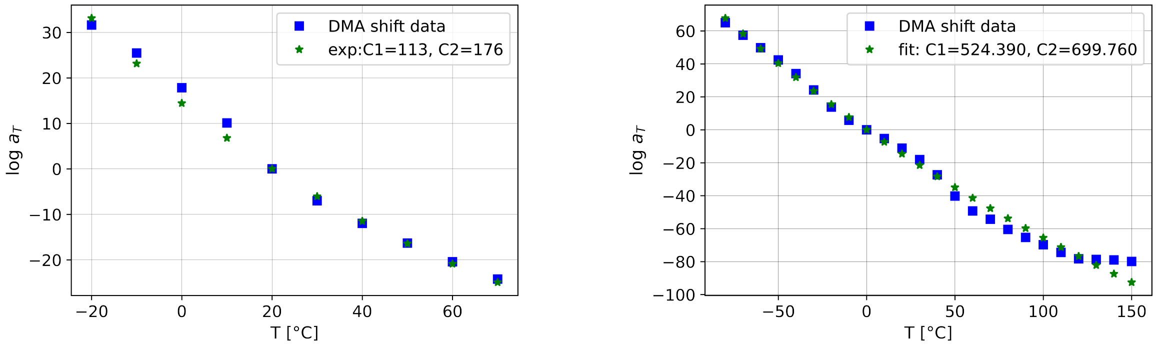

(a) PP BJ380MO

(b) TPU EOS 1301

Figure 12: WLF shift factor curve fits.

To reduce the number of parameters in the optimisation problem, e_i are fixed to be the values of decades, i.e., $..., 0.1, 0, 10, ...$. Also, the number of branches is assumed to be 1 per decade in the master curve. Then, the following non-linear least squares objective function is constructed subject to certain bounds on the parameters for the optimisation problem,

$$\min_{E_\infty,\, E_i\, \in \mathbb{R}^N} F(E_\infty,\, E_i) \equiv \sum_{i=1}^{N} \left(\frac{E(w_j)}{E_j} - 1 \right)^2 \quad \text{with } E_k > 0\,, \qquad k = 1, ..., N\,. \tag{92}$$

solved using the scipy optimisation module [65]. In the numerator of the above objective function, $E(t_j)$ is the predicted value from Eq. (91) for assumed time samples and E_j is the observed value from the master curve. In this work, 27 branches are chosen each for polypropylene and TPU, listed in Tables D.3 and D.8 in Appendix D. The Prony series fit obtained for the parameters for the two materials is compared to their respective master curves in Figs. 13a and 13b.

5.2.2. Calibration of TVE and TVP Parameters

Referring to Table 1, the remaining parameters are to be calibrated from the uniaxial experiments explained before. Firstly, the quasi-nonlinear viscoelastic parameters describe the initial slope of the stress-strain curve and this shape is material-specific. To reduce the number of parameters in Eqs. (43-44), the volumetric and deviatoric parameters are made equal, i.e., $V_{tj} = D_{tj}$ and

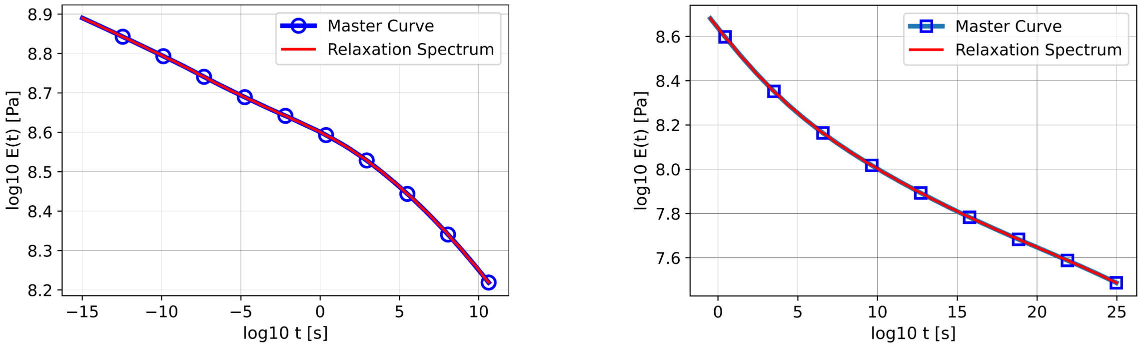

(a) PP BJ380MO (b) TPU EOS 1301

Figure 13: Relaxation spectra curve fits.

$V_{cj} = D_{cj}$. Secondly, in thermoviscoplasticity, the isotropic hardening parameters are assumed to be independent of the strain rate which justifies the form in Eqs. (86). The nonlinear viscoelastic region at low deformations is the focus of this calibration stage to capture dramatically different behaviours in tension and compression states. The stress values at failure encountered in all cases are ignored as damage is not modelled in this study. The tension-compression regularisation constant, ξ, in the logistic function introduced in Eqs. (42) is assumed to be a certain value depending on the level of moduli asymmetry encountered.

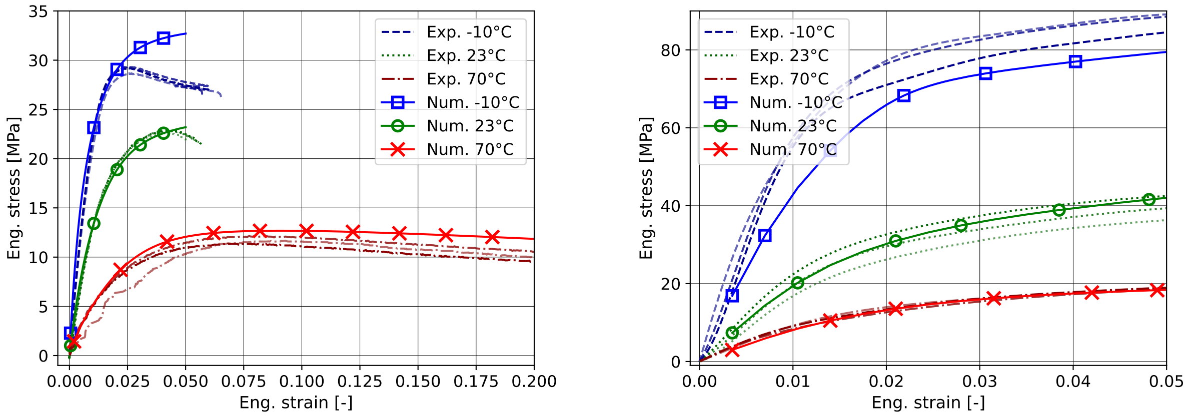

(a) Tension (b) Compression

Figure 14: Calibration: Quasi-steady stress-strain response of PP BJ380MO at varying temperature.

For polypropylene, observing the curves in Fig. 14, a sigmoid-like shape is deemed sufficient and, $V_{t4}, V_{t5}, V_{c4}, V_{c5}$ and their deviatoric counterparts are set to zero. V_{t3} and D_{t3} are retained to prevent geometric softening at high elongations in tension. Regarding the bulk and shear moduli, due to the lack of data and the variability encountered in tension-compression curves, Poisson's ratio is assumed to be 0.33. This relatively low value is intended to prioritise the initial bulk and shear moduli at low temperatures, −10°C, refer to [52] for the variation of Poisson's ratio of polypropylene with temperature. This choice is driven by the highest variation in moduli encountered at −10°C in experimental data. Using the tension-compression experiments at 3 temperatures, the values of the quasi-nonlinear viscoelasticity at the corresponding Maxwell branches are predicted and the rest are linearly interpolated. These values are listed in Table D.4. The motivation for using the quasi-nonlinear viscoelastic model is to capture the highly nonlinear slope with low residual strains upon unloading in the form of strain-dependent moduli, and the large asymmetry encountered in the tension-compression moduli. In thermoviscoplasticity, the asymmetric yield strengths and dependence on the pressure state justify the power-yield function. Further assumptions are made with regards to the plastic Poisson's ratio set to 0.4, a choice influenced by a significant shear-dominated plastic flow [7], the power-yield parameter set to 1.5 to capture the large asymmetry in yield strengths and due to the experiments lacking any re-hardening stage following peak stresses kinematic hardening is ignored for this material. Using the same experimental curves, the isotropic hardening parameters, yield strengths, hardening moduli and the pressure dependency of yielding are subsequently determined and listed in Table D.5 in Appendix D.

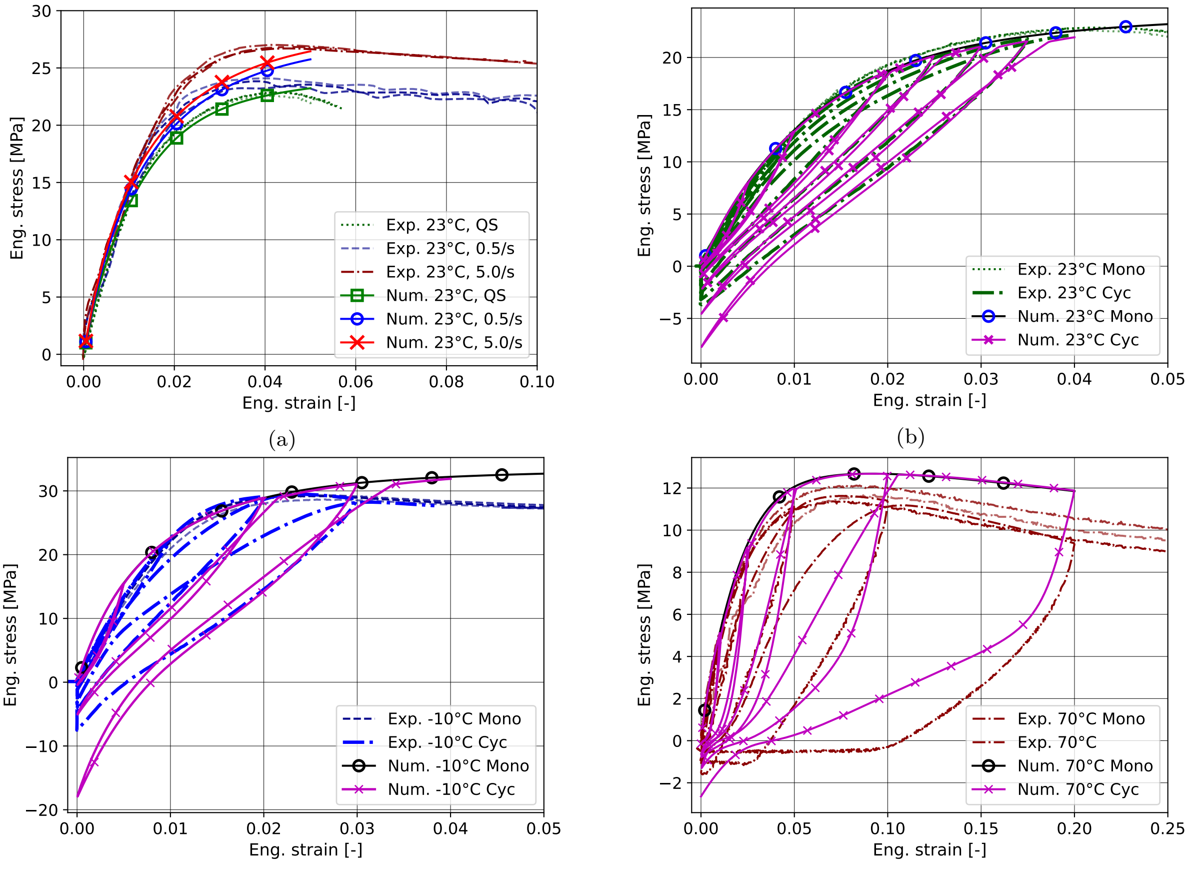

(a)

(b)

(c)

(d)

Figure 15: Tensile stress-strain response of PP BJ380MO at (a) variable strain rates monotonic loading at room temperature and (b,c,d) quasi-steady cyclic loading at 23, -10 and 70°C, with corresponding Mullins' parameters set to 0.5, 0.6 and 0.95, respectively. Terms *mono* refers to monotonic and *cyc* to cycling loadings, respectively.

The Mullins' parameter at 3 temperatures is subsequently determined by observing the unloading curves in cyclic loading experiments. Since the slopes in unloading are the lowest at around 23°C, i.e., the glass transition region, Mullins' parameter is smallest here. However, this trough-like temperature function shape cannot be described by a negative exponential function; hence, this temperature dependency is ignored due to a lack of additional information. All the calibration hence performed leads to the numerical engineering stress-strain curves for PP BJ380MO reported in Figs. 14-15. The highly non-linear regions at low deformations relevant to the quasi-nonlinear viscoelastic region are clearly captured as well as the highly asymmetric peak loads and the moduli inferred from the experimental data in tension and compression. For cycling loading in numerical simulations, it is assumed that the unloading is performed at quasi-steady strain rates and no dwell time is implemented for convenience. The value of the tension-compression regularisation parameter (ξ) is set to 1000 presumably due to high elastic moduli asymmetry. This choice is justified later in Section 5.2.3.

In Fig. 14a the tensile numerical response at -10°C is less accurate as post-peak softening brought about by plastic strain is not modelled here. Fig. 14b shows the relatively higher stresses at the same strain rate and temperatures in compression being modelled sufficiently well. The compressive response at higher strains is ignored for this material because the log-like behaviour presents itself with no further hardening sustainable by the yield function indicating a need for damage to model the flat region in the experimental curves noted in Fig. 14b. The behaviour at higher strain rates in Fig. 15a is slope-accurate but the response at 5/s is found to be underestimated at even low to moderate deformations. Further investigation is required to model an accurate response to higher strain rates and at higher deformations as a clear shift from failure at moderate deformations to post-peak softening, prolongated hardening and failure is evident at higher strain rates. Furthermore, the response in cyclic loading in Figs. 15b-15d, is captured well using the simplified Mullins' like effect.

For TPU, the assumed constant Poisson's ratio is 0.4, despite some sources reporting 0.42 [66] and as high as 0.48 [67]. This assumption allows the simulation of high strains in compression (approx. 0.65) without encountering incompressibility issues. Noting the curves in tension in Figs. 16a, to provide additional stiffness at large deformations V_{t4}, V_{t5} and their deviatoric counterparts are needed to produce a tangent hyperbolic shape along with the sigmoid at small deformations. In compression, see Fig. 16c, V_{c5} is not required since the behaviour can be easily captured with a sigmoid-like shape and the logarithmic strain measure. However, since the data is only available at a single temperature, the quasi-nonlinear viscoelastic parameters are assumed to be equal in all Maxwell branches. These values are listed in Table D.9 in Appendix D. In thermoviscoelasticity, the plastic Poisson's ratio is assumed again to be 0.4. Since TPU is elastomeric at room temperature, the yielding is expected to be shear-dominated and the power yield parameter is set to 3.5. The isotropic and kinematic hardening and viscosity models are established using the tension and compression experiments at a single strain rate, reported in Table D.10 in Appendix D.

This calibration leads to the numerical results presented in Figs. 16 and 17. The current model

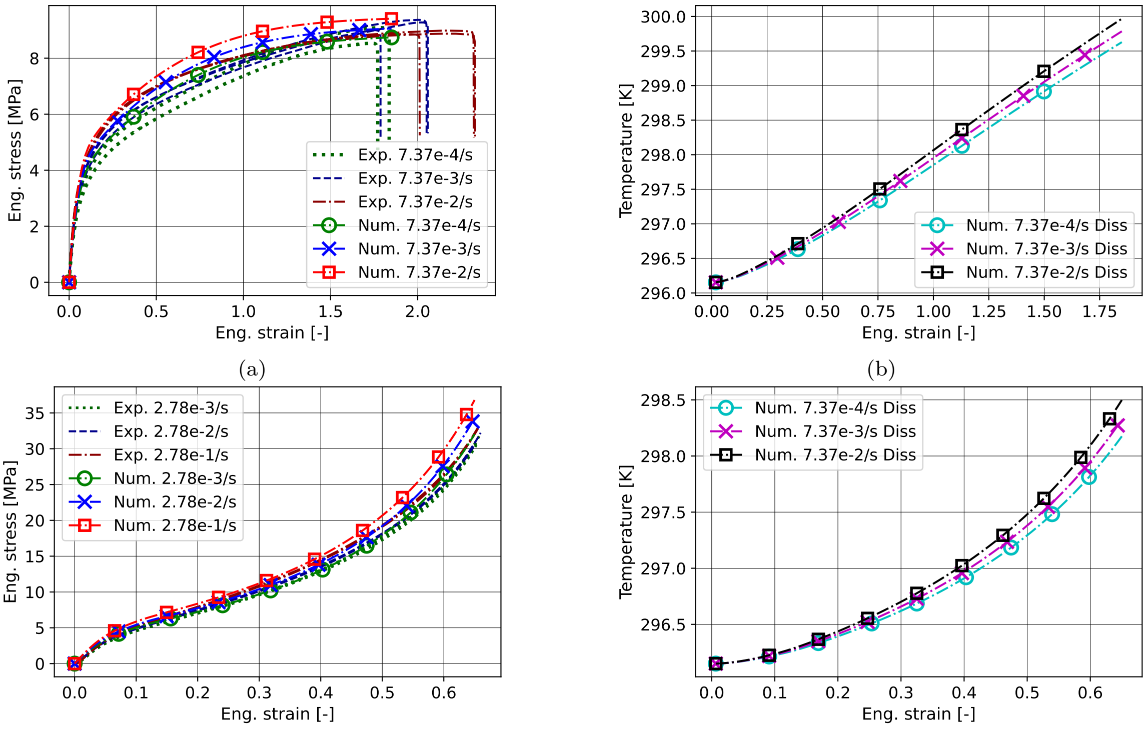

(a) (b)

(c) (d)

Figure 16: Calibration: Monotonic stress-strain response of EOS TPU 1301 at room temperature and variable strain rates in (a) tension and (c) compression, and corresponding temperature increments in (b) and (d), where *diss* implies dissipation.

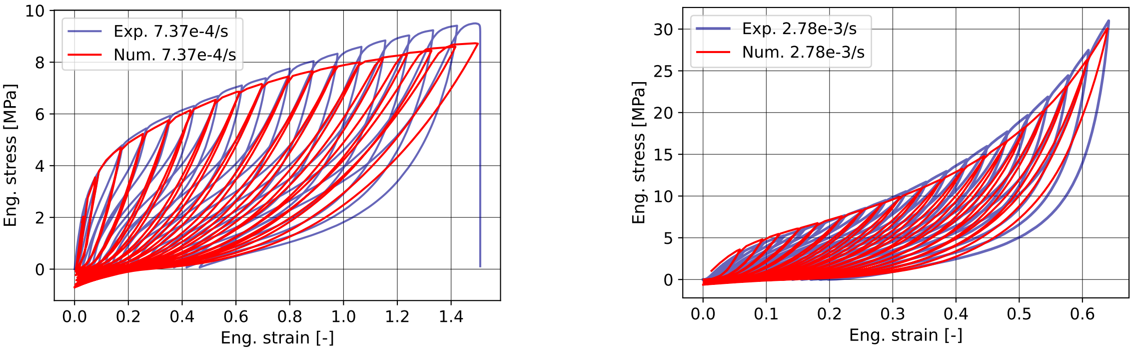

(a) (b)

Figure 17: Calibration: Cyclic stress-strain response of EOS TPU 1301 at room temperature, different strain rates and Mullins' parameter set to 0.99 in (a) tension and (b) compression.

over-predicts the strain-rate effect, see Figs. 16a and 16c, due to a largely viscoelasticity-based model instead of a hyperelastic model, refer to [68, 37]. However, the nature of the curve is well-predicted in both tension and compression. Furthermore, the monotonic loading cases induce self-heating as shown in Figs. 16b and 16d. However, these temperature increments cannot be verified due to a lack of measurements for the bulk testing used for calibration. Any induced softening is however included in the response. Regardless, a similar order of temperature increments has been found in [69]. In cyclic loading, unloadings in simulations are performed until zero strain unlike the experiments as the residual strain is found to be fairly low, see Fig. 17, where the unloading curves are inaccurate possibly due to the simplified Mullins'-like effect adopted in this work. The intention then is to dissipate the mechanical energy using the Mullins' dissipation term and plastic power which necessitates a high Mullins' parameter assumed to be 0.99. Its temperature dependency is ignored due to a lack of data. Regardless, general trends of thermomechanical response are captured fairly well. The value of the tension-compression regularisation parameter (ξ), justified later, is set to 100 owing to the asymmetry in moduli showing itself only at large deformations in tension.

5.2.3. Value of Regularisation Constant in Quasi-nonlinear TVE

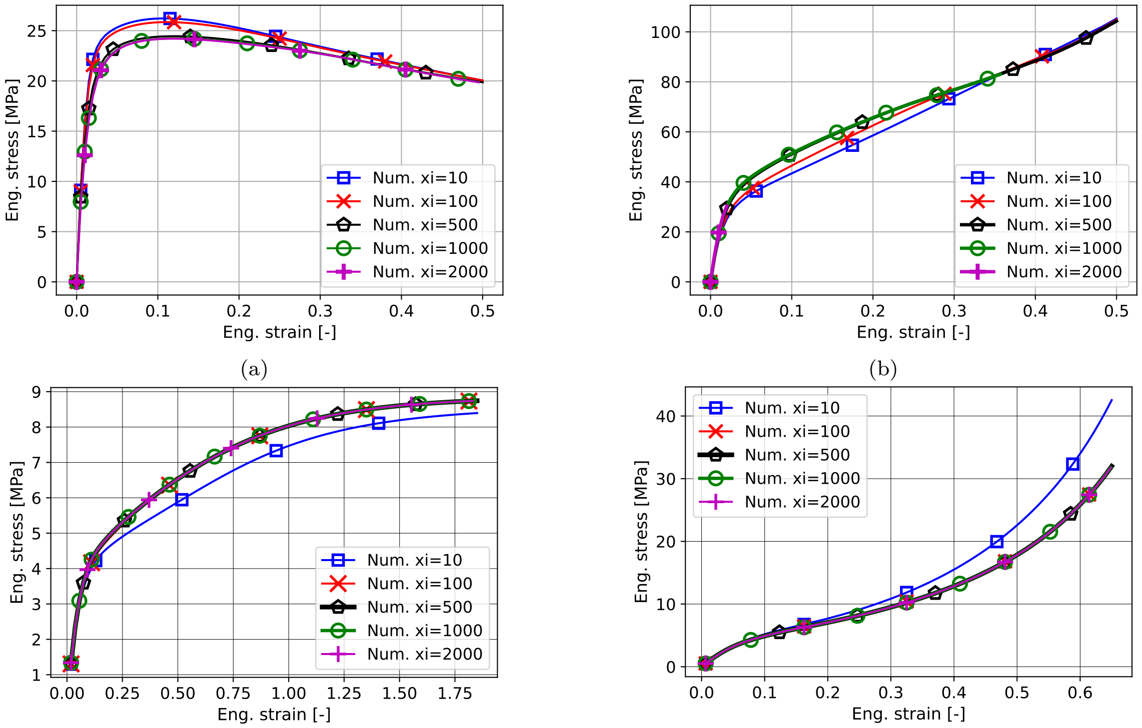

(a) (b)

(c) (d)

Figure 18: Monotonic stress-strain response at room temperature and constant strain rate of PP BJ380MO in (a) tension and (b) compression, and EOS TPU 1301 in (c) tension and (d) compression.

Uniaxial monotonic simulations using the material parameters previously calibrated for the two materials are performed at an initial temperature of 23°C and low strain rates in compression and tension to test the stress response at different values of the tension-compression regularisation parameter ξ. The plots for PP in Figs. 18a and 18b show that at lower elongations the curves converge at $\xi > 10$. At higher elongations, all curves converge which is due to the saturation of the sigmoid-like functions in Eqs. (43-44) and the dominance of tension-compression regularisation function. However, as this function is expected to produce a sharp peak in its derivatives, the tangents may lead to numerical issues in a numerical simulation as seen in Fig. 18b where the $\xi = 2000$ is numerically unstable. For polypropylene BJ380MO, ξ is consequently set to 1000 to account for a large asymmetry in moduli at lower elongations. For TPU, however, see Figs. 18c and 18d, all curves converge for $\xi > 10$ and consequently, ξ is set to 100.

6. Constitutive Model Verification and Validation

In this section, numerical simulations using the material parameters previously calibrated for TPU EOS 1301 are performed on the hollow dumbbell model using the geometric specifications in Fig. 9 at 23°C and 1°/s twist rate in torsion to verify the stress response and energy dissipated due to plasticity with and without the correction for coaxiality introduced in Section 3.4. The geometry is meshed using 2^{nd}-order 10-noded tetrahedral elements in an unstructured and coarse manner with a characteristic length of 2.5mm. For the boundary conditions, the temperature is fixed at 23°C, and assuming the cylindrical axis is parallel to the vertical direction, the curved surface of the lower bell is completely fixed and the curved surface of the upper bell is rotated at a twist rate of 1°/s by translating the nodes of the surface at every time-step through a planar coordinate transformation equivalent to rotation about the cylindrical axis. The moment about the vertical axis is sought for comparison, the following formula is used:

$$M_y = \sum_{i=1}^{N_n} \left(-x^i F_z^i + z^i F_x^i\right) \ , \tag{93}$$

where i is the i^{th} node on the curved surface of the upper bell where the displacement boundary condition is applied, x^i and z^i are the x and z Cartesian coordinates as applied and, F_x^i and F_z^i are the lateral internal forces due to the corresponding shear stresses, τ_{xy} and τ_{yz} arising from the applied torsion [70].

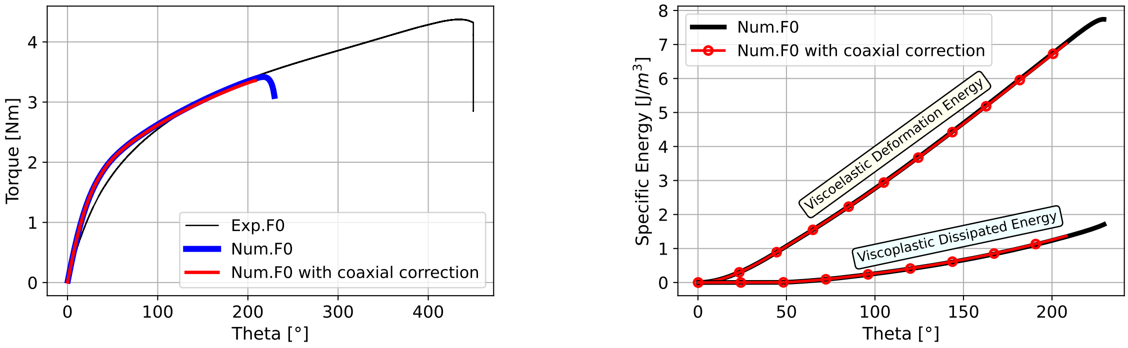

(a) (b)

Figure 19: Comparison between torsion simulations with and without coaxiality correction at 23°C and 1°/s twist rate.

The simulation is successively conducted accounting for the coaxiality correction reported in Section 3.4, and neglecting it. The resulting torques are reported in Fig. 19a in comparison with the experimental values corresponding to 1°/s. Numerical predictions closely follow the experimental curve up to the buckling of the cylinder illustrated in Fig. 20. At this stage, since our implementation does not include self-contact of the inner-wall, the simulation stops, while the experimental test proceeds with a torsion of the buckled and self-contacting inner wall of the cylinder, which allows the structure to sustain further loading in the post-buckling state as illustrated in Fig. 10b.

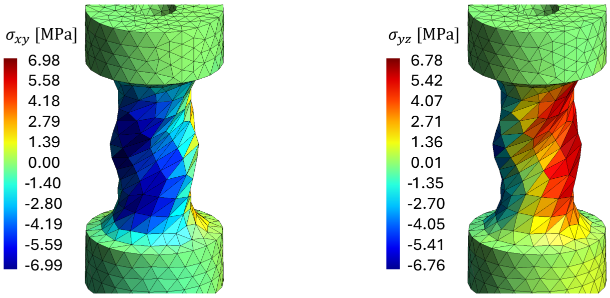

(a) Shear stress XY

(b) Shear stress YZ

Figure 20: Torsion buckling shape - shear stress distributions.

The discrepancy is thus not due to the constitutive model but to the extreme deformation (more than one turn) of the experimental setup which corresponds to the torsion of a self-contacting squeezed cylinder.

The simulation without the coaxiality correction is allowed to progress a few time-steps into the post-buckling state to visualise the buckling mode and the corresponding twist angle with regards to the experiment. With the correction, however, because of the additional computational expenditure to optimise for the correct set of rotated eigenvalues the simulation is stopped at the onset of buckling. As shown in Fig. 19a, the two cases follow the trend of the curve but abruptly fail due to torsion instability that leads to a mode 1 buckling shape, see Fig. 20 corresponding to a twist rate of 1°/s. The slopes at twist angles 200° are equal to the experiment, but the time taken without and with coaxial correction is 19 hours on 4 processors and 14.7 hours on 16 processors, respectively. The latter, to have a similar computational time, requires 4 times as many processors. Also, in Fig. 19b, the viscoelastic deformation and viscoplastic dissipated energies per unit-specific volume are reported and for the two simulations the same values are observed. For practicality, further validation is performed without the coaxial correction which produces similar energy and stress values.

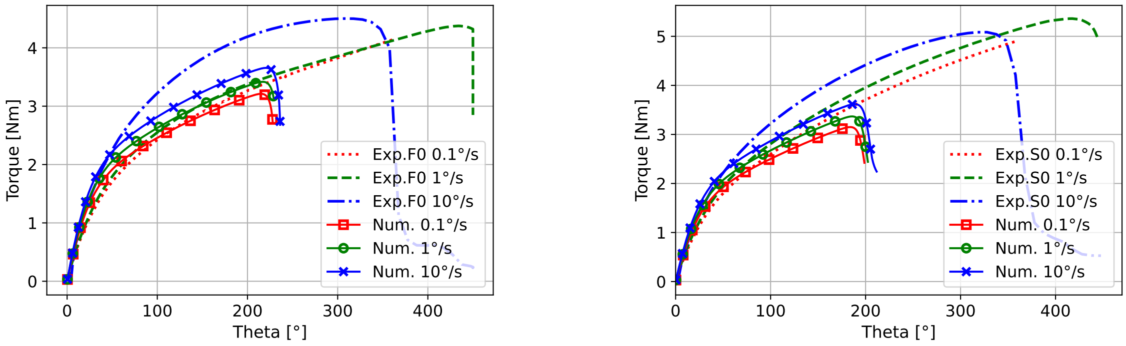

(a)

(b)

Figure 21: Validation of the constitutive model using hollow dumbbell geometry for torsion response of EOS TPU 1301 (a) without and (b) with axial displacement constraint.

Subsequent torsion simulations without the coaxial correction are performed at the twist rates

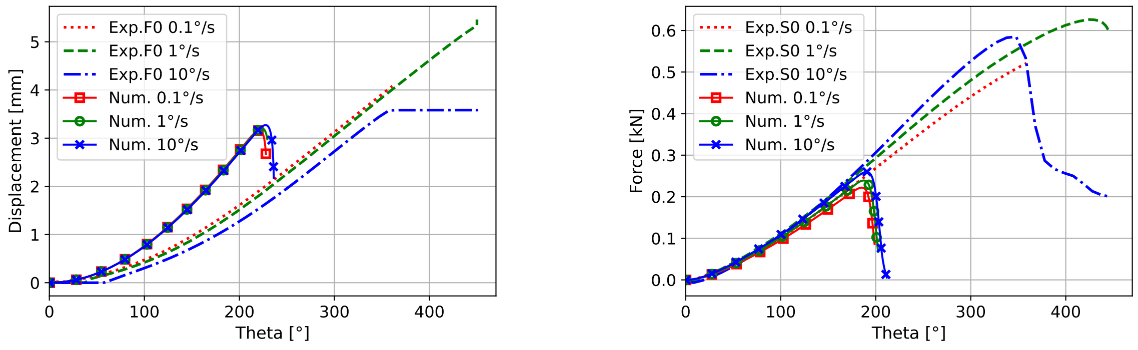

(a)

(b)

Figure 22: Validation of the constitutive model using hollow dumbbell geometry for torsion response of EOS TPU 1301 without and with axial displacement constraint to show (a) Poynting effect and (b) Axial reaction force, respectively.

specified in Fig. 21a. To observe the positive Poynting effect the upper surface is unconstrained in the vertical direction and vice-versa. The results are reported in Figs. 21-22. Again, the torques in Figs. 21a and 21b follow the trend of the curve but abruptly fail due to torsion instability, during which self-contact should be implemented to match the experimental results. The axial force in cases with axial displacement constraint follows the experimental trend in Fig. 22b until instability. The positive Poynting effect in Fig. 22a, however, is over-predicted which requires further investigation.

7. Conclusions and Perspectives

A finite strain quasi-nonlinear thermoviscoelastic and thermoviscoplastic constitutive model with Mullins'-like effect was developed in this work to model large nonlinearities in the elastic regime, tension-compression asymmetry in elastic moduli and yield strengths, and strong hysteresis in unloading. A complete model was presented combining linear viscoelastic theory with time-temperature superposition and non-linear strain-dependent moduli, mixed hardening viscoplasticity using temperature-dependent yield strengths, non-linear Chaboche kinematic hardening, power yield function and Peryzyna-type flow rule. An intuitive methodology was developed to correct non-coaxiality in stress tensors arising from viscoelastic integrals, which despite its numerical expenditure provides a coaxial plastic driving stress and backstress under complex loading scenarios. Overall, the developments are intended to produce a thermomechanically consistent formulation to model the non-linear fully-coupled thermomechanical response encountered in thermoplastic polymers in a wide range of strain rates and temperatures.

The model was calibrated to conventional semicrystalline thermoplastic polymers - polypropylene and thermoplastic polyurethane. The former presented strain-rate and temperature-dependent tension-compression asymmetric moduli, yield strengths, and lower-than-expected unloading stresses, which were captured using the developed constitutive model. The latter material with its elasticity-dominated deformation sustained higher loads in tension under large deformations and presented strong hysteresis in unloading that were captured sufficiently well. 3D printed TPU specimens were experimentally subjected to torsional deformation and then used to establish the applicability of the constitutive model to simulate complex loading scenarios until the apparent onset of failure. The buckling modes due to torsion instability were numerically verified for TPU.

Despite being limited to non-damage cases, the model can be extended to non-local damage formulations such as the one reported in [22]. The thermodynamic foundation developed for Mullins' effect can be adapted to progressive damage as presented in [43]. Furthermore, such a formulation can be used to simulate internal dissipation due to irreversible damage-like phenomena. Lastly, owing to the wide range applications of thermoplastic composites, the developed constitutive model can be readily applied to the resin in multiscale analyses to model phenomena such as thermomechanical fatigue, hyperelasticity and unloading hysteresis of arbitrary non-linearity and self-heating induced damage.

Acknowledgements

This research has been funded by the Walloon Region under the agreement no. 2010092-CARBOBRAKE in the context of the M-ERA.Net Join Call 2020 funded by the European Union under the Grant Agreement no. 958174.

TPU experimental results were obtained in MOAMMM project which has received funding from the H2020-EU.1.2.1.-FET Open Programme project MOAMMM under grant No 862015. Views and opinions expressed are those of the author(s) only and do not necessarily reflect those of the European Union or the European Commission. Neither the European Union nor the granting authority can be held responsible for them.

Computational resources have been provided by the supercomputing facilities of the Consortium des Équipements de Calcul Intensif en Fédération Wallonie Bruxelles (CÉCI).

Data availability

The raw/processed data required to reproduce these findings is available on `https://gitlab.onelab.info/cm3/carbobrake` under the Creative Commons Attribution 4.0 International (CC BY 4.0) licence [71].

References

[1] J Richeton, Said Ahzi, Kenneth S Vecchio, Fengchun C Jiang, and Raghavendra R Adharapurapu. Influence of temperature and strain rate on the mechanical behavior of three amorphous polymers: Characterization and modeling of the compressive yield stress. *International journal of solids and structures*, 43(7-8):2318–2335, 2006.

[2] Jean-Luc Bouvard, David K Francis, Mark A Tschopp, EB Marin, DJ Bammann, and MF Horstemeyer. An internal state variable material model for predicting the time, thermomechanical, and stress state dependence of amorphous glassy polymers under large deformation. *International Journal of Plasticity*, 42:168–193, 2013.

[3] Stéphanie Djukic, Anthony Bocahut, Jérôme Bikard, and Didier R Long. Mechanical properties of amorphous and semi-crystalline semi-aromatic polyamides. *Heliyon*, 6(4), 2020.

[4] Joakim Johnsen, Frode Grytten, Odd Sture Hopperstad, and Arild Holm Clausen. Influence of strain rate and temperature on the mechanical behaviour of rubber-modified polypropylene and cross-linked polyethylene. *Mechanics of Materials*, 114:40–56, 2017.

[5] Ruyue Song, Michael Berer, and Anastasia Muliana. Mechanical responses of semi-crystalline thermoplastic polymers at various temperatures. *International Journal of Solids and Structures*, 238:111398, 2022.

[6] Aleksey D Drozdov and J deC Christiansen. Tension–compression asymmetry in the mechanical response of hydrogels. *Journal of the Mechanical Behavior of Biomedical Materials*, 110:103851, 2020.

[7] Elhem Ghorbel. A viscoplastic constitutive model for polymeric materials. *International Journal of Plasticity*, 24(11):2032–2058, 2008.

[8] D Rittel and A Dorogoy. A methodology to assess the rate and pressure sensitivity of polymers over a wide range of strain rates. *Journal of the Mechanics and Physics of Solids*, 56(11):3191–3205, 2008.

[9] Zhihong Liang, Jian Li, Xuelian Zhang, and Qianhua Kan. A viscoelastic-viscoplastic constitutive model and its finite element implementation of amorphous polymers. *Polymer Testing*, 117:107831, 2023.

[10] Stuart Hillmansen, S Hobeika, RN Haward, and PS Leevers. The effect of strain rate, temperature, and molecular mass on the tensile deformation of polyethylene. *Polymer Engineering & Science*, 40(2):481–489, 2000.

[11] D Barba, Angel Arias, and Daniel Garcia-Gonzalez. Temperature and strain rate dependences on hardening and softening behaviours in semi-crystalline polymers: Application to peek. *International Journal of Solids and Structures*, 182:205–217, 2020.

[12] Meredith N Silberstein and Mary C Boyce. Constitutive modeling of the rate, temperature, and hydration dependent deformation response of nafion to monotonic and cyclic loading. *Journal of Power Sources*, 195(17):5692–5706, 2010.

[13] Jorgen S Bergström and Mary C Boyce. Constitutive modeling of the large strain time-dependent behavior of elastomers. *Journal of the Mechanics and Physics of Solids*, 46(5):931–954, 1998.

[14] AD Drozdov and J deC Christiansen. Mullins' effect in semicrystalline polymers: experiments and modeling. *Meccanica*, 46:359–370, 2011.

[15] Daniel Garcia-Gonzalez, Ramón Zaera, and A Arias. A hyperelastic-thermoviscoplastic constitutive model for semi-crystalline polymers: application to peek under dynamic loading conditions. *International Journal of Plasticity*, 88:27–52, 2017.

[16] Rebecca N Haward and G 1 Thackray. The use of a mathematical model to describe isothermal stress-strain curves in glassy thermoplastics. *Proceedings of the Royal Society of London. Series A. Mathematical and Physical Sciences*, 302(1471):453–472, 1968.

[17] MC Boyce, S Socrate, and PG Llana. Constitutive model for the finite deformation stress–strain behavior of poly (ethylene terephthalate) above the glass transition. *Polymer*, 41(6):2183–2201, 2000.

[18] C Ovalle Rodas, Fahmi Zaïri, and Moussa Naït-Abdelaziz. A finite strain thermo-viscoelastic constitutive model to describe the self-heating in elastomeric materials during low-cycle fatigue. *Journal of the Mechanics and Physics of Solids*, 64:396–410, 2014.

[19] Joakim Johnsen, Arild Holm Clausen, Frode Grytten, Ahmed Benallal, and Odd Sture Hopperstad. A thermo-elasto-viscoplastic constitutive model for polymers. *Journal of the Mechanics and Physics of Solids*, 124:681–701, 2019.

[20] Pei Hao, Vikram Laheri, Ziwei Dai, and FA Gilabert. A rate-dependent constitutive model predicting the double yield phenomenon, self-heating and thermal softening in semi-crystalline polymers. *International Journal of Plasticity*, 153:103233, 2022.

[21] Marie-Christine Reuvers, Birte Boes, Sebastian Felder, Tim Brepols, Sameer Kulkarni, Klara Loos, Michael Johlitz, Alexander Lion, and Stefanie Reese. Semi-crystalline polymers at finite strains: A thermo-coupled constitutive model for varying degrees of crystallinity and temperatures. *PAMM*, 23(1):e202200162, 2023.

[22] V.D. Nguyen, F. Lani, T. Pardoen, X.P. Morelle, and L. Noels. A large strain hyperelastic viscoelastic viscoplastic damage constitutive model based on a multimechanism nonlocal damage continuum for amorphous glassy polymers. *International Journal of Solids and Structures*, 96:192–216, 2016.

[23] Francis Praud, George Chatzigeorgiou, Jérôme Bikard, and Fodil Meraghni. Phenomenological multi-mechanisms constitutive modelling for thermoplastic polymers, implicit implementation and experimental validation. *Mechanics of Materials*, 114:9–29, 2017.

[24] H Schiessel, R Metzler, A Blumen, and TF0921 Nonnenmacher. Generalized viscoelastic models: their fractional equations with solutions. *Journal of physics A: Mathematical and General*, 28(23):6567, 1995.

[25] RS Lakes and R Vanderby. Interrelation of creep and relaxation: a modeling approach for ligaments. 1999.

[26] Kevin L Troyer and Christian M Puttlitz. Nonlinear viscoelasticty plays an essential role in the functional behavior of spinal ligaments. *Journal of biomechanics*, 45(4):684–691, 2012.

[27] Wenqiang Liu, Kevin M Labus, Matt Ahern, Kristen LeBar, Reza Avazmohammadi, Christian M Puttlitz, and Zhijie Wang. Strain-dependent stress relaxation behavior of healthy right ventricular free wall. *Acta biomaterialia*, 152:290–299, 2022.

[28] Erhard Krempl and Fazeel Khan. Rate (time)-dependent deformation behavior: an overview of some properties of metals and solid polymers. *International Journal of Plasticity*, 19(7):1069–1095, 2003.

[29] Muralidhar Reddy Gudimetla and Issam Doghri. A finite strain thermodynamically-based constitutive framework coupling viscoelasticity and viscoplasticity with application to glassy polymers. *International Journal of Plasticity*, 98:197–216, 2017.

[30] Chao Yu, Guozheng Kang, Kaijuan Chen, and Fucong Lu. A thermo-mechanically coupled nonlinear viscoelastic–viscoplastic cyclic constitutive model for polymeric materials. *Mechanics of Materials*, 105:1–15, 2017.

[31] A. Krairi, I. Doghri, J. Schalnat, G. Robert, and W. Van Paepegem. Thermo-mechanical coupling of a viscoelastic-viscoplastic model for thermoplastic polymers: Thermodynamical derivation and experimental assessment. *International Journal of Plasticity*, 115:154–177, 2019.

[32] Seishiro Matsubara, Kenjiro Terada, Ryusei Maeda, Takaya Kobayashi, Masanobu Murata, Takuya Sumiyama, Kenji Furuichi, and Chisato Nonomura. Viscoelastic-viscoplastic combined constitutive model for glassy amorphous polymers under loading/unloading/no-load states. *Engineering Computations*, 37(5):1703–1735, 2020.

[33] Pericles RP Carvalho, Humberto B Coda, and Rodolfo AK Sanches. A large strain thermodynamically-based viscoelastic–viscoplastic model with application to finite element analysis of polytetrafluoroethylene (ptfe). *European Journal of Mechanics-A/Solids*, 97:104850, 2023.

[34] P Narayanan, R Pramanik, and A Arockiarajan. A hyperelastic viscoplastic damage model for large deformation mechanics of rate-dependent soft materials. *European Journal of Mechanics-A/Solids*, 98:104874, 2023.

[35] Alexander Ricker, Nils Hendrik Kröger, and Peter Wriggers. Comparison of discontinuous damage models of mullins-type. *Archive of Applied Mechanics*, 91(10):4097–4119, 2021.

[36] David Cichra, Pablo Alexei Gazca-Orozco, Vit Pruvsa, and Karel Tuma. A thermodynamic framework for non-isothermal phenomenological models of isotropic mullins effect. *Proceedings of the Royal Society A*, 479(2272):20220614, 2023.

[37] Sergio I Reyes, Michalis F Vassiliou, and Dimitrios Konstantinidis. Experimental characterization and constitutive modeling of thermoplastic polyurethane under complex uniaxial loading. *Journal of the Mechanics and Physics of Solids*, page 105582, 2024.

[38] LR Herrmann. A numerical procedure for viscoelastic stress analysis. In *Seventh Meeting of ICRPG Mechanical Behavior Working Group, Orlando, FL, 1968*, 1968.

[39] Stefanie Reese and Sanjay Govindjee. A theory of finite viscoelasticity and numerical aspects. *International journal of solids and structures*, 35(26-27):3455–3482, 1998.

[40] Bingfeng Fan and David O Kazmer. Low-temperature modeling of the time-temperature shift factor for polycarbonate. *Advances in Polymer Technology: Journal of the Polymer Processing Institute*, 24(4):278–287, 2005.

[41] Richard A Schapery. On the characterization of nonlinear viscoelastic materials. *Polymer Engineering & Science*, 9(4):295–310, 1969.

[42] Robert S. Chambers. Numerical integration of the hereditary integrals in a viscoelastic model for glass. *Journal of the American Ceramic Society*, 75(8):2213–2218, 1992.

[43] Fei Shen, Guozheng Kang, Yee Cheong Lam, Yujie Liu, and Kun Zhou. Thermo-elastic-viscoplastic-damage model for self-heating and mechanical behavior of thermoplastic polymers. *International Journal of Plasticity*, 121:227–243, 2019.

[44] J.-L. Chaboche. Cyclic Viscoplastic Constitutive Equations, Part I: A Thermodynamically Consistent Formulation. *Journal of Applied Mechanics*, 60(4):813–821, 12 1993.

[45] Lallit Anand, Nicoli M Ames, Vikas Srivastava, and Shawn A Chester. A thermo-mechanically coupled theory for large deformations of amorphous polymers. part i: Formulation. *International Journal of Plasticity*, 25(8):1474–1494, 2009.

[46] Juan C. Simo Gerhard A. Holzapfel. A new viscoelastic constitutive model for continuous media at finite thermomechanical changes. *International Journal of Solids and Structures*, 33:3019–3034, 1996.

[47] R. Xiao, J. Choi, N. Lakhera, C.M. Yakacki, C.P. Frick, and T.D. Nguyen. Modeling the glass transition of amorphous networks for shape-memory behaviors. *Journal of the Mechanics and Physics of Solids*, 61:1612–1635, 2013.

[48] Raymond W. Ogden Giuseppe Saccomandi. *Mechanics and Thermomechanics of Rubberlike Solids*, chapter 1. Springer-Verlag Wien GmbH, Kassel, Germany, 1st edition, 2004.

[49] John D. Ferry. *Viscoelastic Properties of Polymers*, chapter 11. John Wiley and Sons, Inc, Madison, Wisconsin, 1st edition, 1980.

[50] Robert L Taylor, Karl S Pister, and Gerald L Goudreau. Thermomechanical analysis of viscoelastic solids. *International journal for numerical methods in engineering*, 2(1):45–59, 1970.

[51] M. Fernanda P. Costa and C. Ribeiro. Parameter estimation of viscoelastic materials: A test case with different optimization strategies. *AIP Conference Proceedings*, 1389(1):771–774, 2011.

[52] Daniel Tscharnuter, Michael Jerabek, Zoltan Major, and Reinhold W Lang. Time-dependent poisson's ratio of polypropylene compounds for various strain histories. *Mechanics of time-dependent materials*, 15:15–28, 2011.

[53] Ujwal Kishore Jinaga, Kepa Zulueta, Aizeti Burgoa, Lucia Cobian, Ubiratan Freitas, Michael Lackner, and Zoltan Major. Supplementary material for "a consistent finite-strain thermo-mechanical quasi-nonlinear-viscoelastic viscoplastic constitutive model for thermoplastic polymers.".

[54] Piotr Perzyna. Thermodynamic theory of viscoplasticity. volume 11 of *Advances in Applied Mechanics*, pages 313–354. Elsevier, 1971.

[55] AR Melro, PP Camanho, FM Andrade Pires, and ST Pinho. Micromechanical analysis of polymer composites reinforced by unidirectional fibres: Part i–constitutive modelling. *International Journal of Solids and Structures*, 50(11-12):1897–1905, 2013.

[56] Borealis GmbH. *Product Data Sheet Polypropylene BJ380MO*, 2017.

[57] EOS GmbH. *Material Data Sheet Thermoplastic Polyurethane EOSTPU1301*, 2024.

[58] Zoltan Major, Michael Lackner, Anna Hössinger-Kalteis, and Thomas Lück. Characterization of the fatigue behavior of sls thermoplastics. *Procedia Structural Integrity*, 34:191–198, 2021.

[59] Moammm open data repository. `http://gitlab.uliege.be/moammm`, 2023.

[60] Netzch polymers tpu data. `https://polymers.netzsch.com/Materials/Details/48`, 2023.

[61] EOS GmbH. *Material Data Sheet Thermoplastic Polyurethane EOSTPU1301 (Laser Sintered)*, 2023.

[62] Busra Cetiner, Gulayse Sahin Dundar, Yusuf Yusufoglu, and Burcu Saner Okan. Sustainable engineered design and scalable manufacturing of upcycled graphene reinforced polylactic acid/polyurethane blend composites having shape memory behavior. *Polymers*, 15(5):1085, 2023.

[63] Alan S Wineman. The poynting effect in elastomeric bars undergoing chemo-mechanical evolution. *Mathematics and Mechanics of Solids*, 26(5):683–693, 2021.

[64] D. Burkat, R. Jamarani, M. Maric, and R. L. Leask. Development of a time temperature superposition program. `https://github.com/dburkat/Master-curve-project.git`, 2018.

[65] Virtanen et al. Fundamental algorithms for scientific computing in python. *Nature Methods*, 17:261–272, 2020.

[66] Sofiane Guessasma, Khaoula Abouzaid, Sofiane Belhabib, David Bassir, and Hedi Nouri. Interfacial behaviour in polymer composites processed using droplet-based additive manufacturing. *Polymers*, 14(5):1013, 2022.

[67] Mehmet Aladag, Monika Bernacka, Magdalena Joka-Yildiz, Wojciech Grodzki, Przemysław Zamojski, and Izabela Zgłobicka. Reverse engineering of parts with asymmetrical properties using replacement materials. *acta mechanica et automatica*, 16(3), 2022.

[68] Penghao Pei, Yueming Du, Yinggang Miao, and Tao Suo. Novel hyper-viscoelastic approach to modelling elastomer mechanic behaviour with relaxation spectrum. *Polymer Testing*, 133:108375, 2024.

[69] Jie Yang, Zisheng Liao, Deepak George, Mokarram Hossain, and Xiaohu Yao. Incorporation of self-heating effect into a thermo-mechanical coupled constitutive modelling for elastomeric polyurethane. *Giant*, 18:100278, 2024.

[70] James P Smith. Highly accurate beam torsion solutions using the p-version finite element method. Technical report, 1996.

[71] Ujwal Kishore Jinaga, Kepa Zulueta, Aizeti Burgoa, Lucia Cobian, Ubiratan Freitas, Michael Lackner, and Zoltan Major. Data of “a consistent finite-strain thermomechanical quasi-nonlinear-viscoelastic viscoplastic constitutive model for thermoplastic polymers.”, November 2024.

Appendix A. Details of Thermoviscoelasticity

Appendix A.1. Viscoelastic Free Energy

The free energy contribution of the hyperelastic branch in the Maxwell model is approximated to be regularised as given below:

$$
\begin{aligned}
\widehat{\psi}_\infty &= K_{\infty 0}\left(f_{\text{reg}}\int_0^{\operatorname{tr}\mathbf{E}_{\text{eff}}} A_{t\infty}\operatorname{tr}\mathbf{E}'_{\text{eff}}\,d(\operatorname{tr}\mathbf{E}'_{\text{eff}}) + C_{0\infty}\,(1-f_{\text{reg}})\int_0^{\operatorname{tr}\mathbf{E}_{\text{eff}}} A_{c\infty}\operatorname{tr}\mathbf{E}'_{\text{eff}}\,d(\operatorname{tr}\mathbf{E}'_{\text{eff}})\right)\ \ldots \\
&\ldots\ + 2\,G_{\infty 0}\left(f_{\text{reg}}\int_0^{\operatorname{dev}\mathbf{E}_e} B_{t\infty}\operatorname{dev}\mathbf{E}'_e : d(\operatorname{dev}\mathbf{E}'_e)\ \ldots\right. \\
&\ldots\qquad\left. + C_{0\infty}\,(1-f_{\text{reg}})\int_0^{\operatorname{dev}\mathbf{E}_e} B_{c\infty}\operatorname{dev}\mathbf{E}'_e : d(\operatorname{dev}\mathbf{E}'_e)\right)\ ,
\end{aligned}
\tag{A.1}
$$

and that of each branch, $\widehat{\psi}_i$,:

$$
\begin{aligned}
\widehat{\psi}_i &= K_{i0}\left(f_{\text{reg}}\int_0^{\operatorname{tr}\mathfrak{E}_i} A_{ti}\operatorname{tr}\mathfrak{E}_i\,d(\operatorname{tr}\mathfrak{E}_i) + C_{0i}\,(1-f_{\text{reg}})\int_0^{\operatorname{tr}\mathfrak{E}_i} A_{ci}\operatorname{tr}\mathfrak{E}_i\,d(\operatorname{tr}\mathfrak{E}_i)\right)\ \ldots \\
&\ldots\ + 2\,G_{i0}\left(f_{\text{reg}}\int_0^{\operatorname{dev}\mathfrak{E}_i} B_{ti}\operatorname{dev}\mathfrak{E}_i\,d(\operatorname{dev}\mathfrak{E}_i)\ \ldots\right. \\
&\ldots\qquad\left. + C_{0i}\,(1-f_{\text{reg}})\int_0^{\operatorname{dev}\mathfrak{E}_i} B_{ci}\operatorname{dev}\mathfrak{E}_i\ : d(\operatorname{dev}\mathfrak{E}_i)\right)\ ,
\end{aligned}
\tag{A.2}
$$

which are analytically exact for $\xi \to \infty$. Explicitly, the integral containing A_{ti} has the following analytical expression:

$$
\begin{aligned}
\int_0^{\operatorname{tr}\mathfrak{E}_i} A_{ti}\operatorname{tr}\mathfrak{E}_i\,d(\operatorname{tr}\mathfrak{E}_i) &= \frac{1}{V_{t1}}\left(\sqrt{V_{t1}\operatorname{tr}\mathfrak{E}_i^2 + V_{t2}} - \sqrt{V_{t2}}\right) + \frac{V_{t3}V_{t4}}{2}\operatorname{tr}\mathfrak{E}_i^2\ldots \\
&\ldots + \frac{V_{t3}}{2V_{t5}}\log\left(\cosh\left(V_{t5}\operatorname{tr}\mathfrak{E}_i^2\right)\right)\ ,
\end{aligned}
\tag{A.3}
$$

and the expressions for the integrals containing A_{ci}, B_{ti} and B_{ci} follow suit. Also, since ξ in f_{reg} is purely a regularisation constant, for $\xi = [0, \infty)$, the above relation for $\widehat{\psi}_i$ is integrable analytically. Then, it is easy to note the energy conjugacy, $\frac{\partial \widehat{\psi}_i}{\partial \operatorname{tr} \boldsymbol{\Gamma}_i} = -\widehat{p}_i$ and $\frac{\partial \widehat{\psi}_i}{\partial \operatorname{dev} \boldsymbol{\Gamma}_i} = -\operatorname{dev} \widehat{\boldsymbol{\tau}}_i$, ignoring the regularisation term derivatives. Also, if the scaling variables, A_i and B_i, are set to 1, $\widehat{\psi}_i$ will have an expression quadratic in terms of $\mathfrak{E}_i$ or indirectly, $\mathbf{E}_e$ and $\boldsymbol{\Gamma}_i$. Such a quadratic expression, ignoring volumetric viscoelastic response, is identical to the free energy relations developed in [46].

Appendix A.2. TTSP - Integration of Shifted Laboratory Time

To evaluate the shifted time-step, the integral in Eq. (47) is solved for the time-step $\Delta t^{\#}$:

$$\Delta t^{\#} \quad = \quad \int_{t^n}^{t^{n+1}} \frac{1}{a_T(\epsilon)} d\epsilon \, . \tag{A.4}$$

For a P-point Gaussian quadrature, consider W_k as the weights and x_k as the nodes or points of the associated Gaussian quadrature rule. For example, $W_k = 1$ and $x_k = \pm\frac{1}{\sqrt{3}}$, for the 2-point rule, which is found to be sufficient in integrating the shift factor [42]. For the intermediate temperatures within a time-step, a linear interpolation may be useful (or quadratic, depending on the availability of an intermediate value from the solver). However, for a midstep approximation the sampling points should be adjusted. This is shown below that $\Delta t^{\#}$ is different for the recursive ($(.)_{\text{rec}}$) and midstep ($(.)_{\text{mid}}$) terms.

$$\Delta t^{\#}\big|_{\text{mid}|\text{rec}} \quad = \quad \left(t^{\#} - s^{\#}\right)\Big|_{s^{\#} = \frac{t^{n+1}+t^n}{2} | t^n}^{t^{\#} = t^{n+1} | t^{n+1}} = \frac{\Delta t}{c_{\text{mid}|\text{rec}}} \sum_{k=1}^{P} W_k \, \exp\left(\frac{C_1 (T(\epsilon(x_k)) - T_{\text{ref}})}{C_2 + T(\epsilon(x_k)) - T_{\text{ref}}}\right) , \tag{A.5}$$

where $c_{\text{mid}} = 4$ and $c_{\text{rec}} = 2$, while $\epsilon(x_k)_{mid} = \frac{3t^{n+1}+t^n}{4} + \frac{\Delta t}{4} x_k$ and $\epsilon(x_k)_{rec} = \frac{t^{n+1}+t^n}{2} + \frac{\Delta t}{2} x_k$.

Appendix A.3. Estimation of the Rotated Bases

Let us consider the form of the rotation tensor, $\mathbf{R}$, provided by Eq. (54). Since $\boldsymbol{N}_k^n$ and $\boldsymbol{N}_k$ form the orthonormal bases for their corresponding 2^{nd} order tensors, the $\mathbf{R}$ constructed above belongs to the Special Orthogonal Group 3 (SO3), i.e., $\mathbf{R}^T\mathbf{R} = \mathbf{R}\mathbf{R}^T = \mathbf{I}$ and $\det \mathbf{R} = 1$. However, in general, there is no canonical representation to the solution of the eigenvalue problem, i.e., for an arbitrary $n-$by$-n$ matrix $\mathbf{A}$ with eigenvalue λ and the corresponding eigenvector v, the solution to the problem $\mathbf{A}v = \lambda v$ yields eigenvalues and their corresponding eigenvectors in no particular order. This implies that in a general loading scenario where the principal directions of the deformation measure possibly change with time, the eigenvectors obtained through the eigenvalue problem solved for the strain tensors from different time-steps cannot be associated with each other, i.e., $\boldsymbol{N}_1^n$ does not necessarily evolve into $\boldsymbol{N}_1$ as the numerical analysis progresses. Therefore, for a general loading case, a constraint is necessary to associate the eigenvectors across time-steps such that the spectral representation of the rotation tensor in Eq. (54) may be constructed. A practical strategy adopted here to produce such an association is a Frobenius norm-based segregation, where

$\boldsymbol{N}_k^n$ are associated with $\boldsymbol{N}_k$ to form an $\mathbf{R}$ that subsequently produces a rotated strain tensor, $\mathbf{E}_e^{n*}$, from the previous time-step using the relation in Eq. (53) which is the least different from $\mathbf{E}_e^n$, i.e., the Frobenius norm of the difference between $\mathbf{E}_e^{n*}$ and $\mathbf{E}_e^n$ is minimal. This is stated below as a minimisation problem:

$$\begin{aligned} &\min_{\boldsymbol{k}} \quad \sqrt{(\mathbf{E}_e^{n*} - \mathbf{E}_e^n) : (\mathbf{E}_e^{n*} - \mathbf{E}_e^n)} \\ &\text{s.t.} \quad \boldsymbol{k} \in 3! \text{ Vectors with uniquely arranged elements 0,1,2} \end{aligned} \tag{A.6}$$

The vector $\boldsymbol{k}$ is the order of the eigenvalues ω_k^n (and the corresponding eigenvectors) that minimises the Frobenius norm stated explicitly above.

Appendix B. Elasto-Plastic Integration Algorithm

The integration Algorithm follows a predictor-corrector scheme and is depicted in the workflow Table B.2 where a suitable tolerance of 1×10^{-6} is chosen to terminate the Newton-Raphson loops.

Appendix B.1. Thermoviscoelastic Predictor

The predictor step entails the evaluation of the stress measure, $\hat{\boldsymbol{\tau}}_e^{\text{pr}}$ as a function of the predicted strain measure, $\mathbf{E}_e^{\text{pr}}$ for null plastic flow using Eq. 59. Overall, the following predictions are made:

$$\mathbf{F}_p^{\text{pr}} = \mathbf{F}_p^n \,, \tag{B.1}$$

$$\mathbf{F}_e^{\text{pr}} = \mathbf{F} \cdot \mathbf{F}_p^{\text{pr}-1} \,, \tag{B.2}$$

$$\mathbf{C}_e^{\text{pr}} = \mathbf{F}_p^{\text{pr}-T} \cdot \mathbf{C} \cdot \mathbf{F}_p^{\text{pr}-1} \,, \tag{B.3}$$

$$\mathbf{E}_e^{\text{pr}} = \frac{1}{2} \ln \mathbf{C}_e^{\text{pr}} \,, \tag{B.4}$$

$$\mathbf{E}_{\text{eff}}^{\text{pr}} = \mathbf{E}_e^{\text{pr}} - 3\alpha_\infty \left(T - T_0\right) \,, \tag{B.5}$$

$$\hat{\boldsymbol{\tau}}_e^{\text{pr}} = \hat{p}^{\text{pr}} \mathbf{I} + \operatorname{dev} \hat{\boldsymbol{\tau}}_e^{\text{pr}} \tag{B.6}$$

$$\boldsymbol{\phi}^{\text{pr}} = \hat{\boldsymbol{\tau}}_e^{\text{pr}} - \mathbf{B}^n \tag{B.7}$$

Then, the yield function F, presented in the Section 4.3, is checked as follows:

$$F(\boldsymbol{\phi}^{\text{pr}}) = a_2 \left(\phi_e^{\text{pr}}\right)^{\alpha} - a_1 \phi_p^{\text{pr}} - a_0 \,. \tag{B.8}$$

If $F \leq 0$ is unsatisfied, the plasticity correction is applied.

Appendix B.2. Thermoviscoplastic Corrector

For an unsatisfied yield condition, i.e., $F(\boldsymbol{\phi}) > 0$, a correction is evaluated and applied to the strain measure. The equivalent plastic strain, γ, and the viscoplastic multiplier, λ, are to be evaluated iteratively for the current time-step such that the extended yield condition is satisfied, i.e., $\bar{F}(\boldsymbol{\phi}) = 0$. The plastic deformation gradient, $\mathbf{F}_p$, is then evaluated through the rate of plastic deformation, $\mathbf{D}_p = \dot{\mathbf{F}}_{\mathbf{p}} \mathbf{F}_p^{-1}$. Here, $\mathbf{D}_p$ is defined through the flow rule in Eq. (66). Using the definition of the plastic potential, P, in Eq. (72), the Flow Normal ($\mathbf{Q}$) is defined and expressed as follows:

$$\mathbf{Q} = \frac{\partial P}{\partial \widehat{\boldsymbol{\tau}}_e} = 3\mathrm{dev}\,\boldsymbol{\phi} + \frac{2\beta}{3}\boldsymbol{\phi}_p\mathbf{I}\,, \tag{B.9}$$

allowing the relation for $\mathbf{D}_p$ to be $\mathbf{D}_p = \dot{\mathbf{F}}_{\mathbf{p}}\mathbf{F}_p^{-1} = \lambda\mathbf{Q}$ that can be integrated to obtain $\mathbf{F}_p$ in the current time interval of $\Delta t = t^{n+1} - t^n$:

$$\mathbf{F}_p = \exp\left[\int_{t^n}^{t^{n+1}} \lambda(t)\mathbf{Q}(t)\,dt\,\right]\mathbf{F}_p^n\,. \tag{B.10}$$

This is simplified using the radial return algorithm where $\mathbf{Q}$ takes its value at the current time-step and drops out of the integral leading to:

$$\mathbf{F}_p = \exp\left(\Gamma\mathbf{Q}\right)\,\mathbf{F}_p^n\,, \tag{B.11}$$

where a new variable (Γ) is defined to be the flow rule parameter obtained from the viscoplastic multiplier λ as follows:

$$\Gamma = \int_{t^n}^{t^{n+1}} \lambda(t)dt = \lambda\Delta t\,. \tag{B.12}$$

Lastly, the increment of the equivalent plastic strain for the current time-step is obtained from the rate equation in Eq. (70):

$$\Delta\gamma = k\Gamma\sqrt{\mathbf{Q}:\mathbf{Q}}\,. \tag{B.13}$$

Corrections are then applied to the elastic deformation gradient, $\mathbf{F}_e$, the right Cauchy and the Hencky strains in the intermediate configuration, $\mathbf{C}_e$, $\mathbf{E}_e$ and $\mathbf{E}_{\text{eff}}$, respectively:

$$\begin{aligned}
\mathbf{F}_e &= \mathbf{F}\mathbf{F}_p^{-1} = \mathbf{F}\cdot\mathbf{F}_p^{n-1}\cdot\left(\exp\left(\Gamma\mathbf{Q}\right)\right)^{-1}\,, && \text{(B.14)}\\
\mathbf{C}_e &= \left(\exp\left(\Gamma\mathbf{Q}\right)\right)^{-T}\cdot\mathbf{C}_e^{\text{pr}}\cdot\left(\exp\left(\Gamma\mathbf{Q}\right)\right)^{-1}\,, && \text{(B.15)}\\
\mathbf{E}_e &= \mathbf{E}_e^{\text{pr}} - \Gamma\mathbf{Q}\,, && \text{(B.16)}\\
\mathbf{E}_{\text{eff}} &= \mathbf{E}_{\text{eff}}^{\text{pr}} - \Gamma\mathbf{Q}\,. && \text{(B.17)}
\end{aligned}$$

The third of the above relations comes from the Eq. (3), which is possible because $\mathbf{Q}$ is symmetric by construction in Eq. (B.9) and commutes with $\mathbf{E}_e$ and $\mathbf{C}_e$ through $\widehat{\boldsymbol{\tau}}_e$. Furthermore, the corrected strain measure of $\mathbf{E}_e$ is then used to estimate the corrected co-rotational Kirchhoff stress, $\widehat{\boldsymbol{\tau}}_e$. Note that because of the scalars, A_i and B_i, in the stress relations defined previously, Eqs. (42), the predicted co-rotational Kirchhoff stress is no longer separable from the correction tensor, $\Gamma\mathbf{Q}$, forgoing the advantage previously used in [22]. This implies that the yield function derivatives soon to be derived for the iterative solution of $\Delta\gamma$ and Γ will be defined directly in terms of the derivatives of $\widehat{\boldsymbol{\tau}}_e$ which are the functions of the inseparable correction tensor, $\Gamma\mathbf{Q}$, making such equations implicit in terms of the correction tensor. The rate of backstress in Eq. (79) is solved using implicit finite differences in time to give the following volumetric and deviatoric contributions of backstress at the current time-step, $\mathbf{B}$:

$$\operatorname{dev}\mathbf{B} = \frac{k^2 H_{\mathbf{B}} \Gamma \operatorname{dev}\mathbf{Q} + \operatorname{dev}\mathbf{B}^{n*}}{C_{\mathbf{B}}} \quad \text{and} \quad \operatorname{tr}\mathbf{B} = \frac{k^2 H_{\mathbf{B}} \Gamma \operatorname{tr}\mathbf{Q} + \operatorname{tr}\mathbf{B}^{n}}{C_{\mathbf{B}}} \,, \tag{B.18}$$

where,

$$C_{\mathbf{B}} = 1 - \frac{m_{\gamma_c}}{H_{\mathbf{B}}} \frac{\partial H_{\mathbf{B}}}{\partial \gamma} \Delta\gamma - \frac{1}{H_{\mathbf{B}}} \frac{\partial H_{\mathbf{B}}}{\partial T} \Delta T \,, \tag{B.19}$$

and $\operatorname{dev}\mathbf{B}^{n*}$ is corrected for coaxiality using the same methodology introduced in Section 3.4. The difference being that the backstress is made coaxial with the flow normal, $\mathbf{Q}$, instead of $\mathbf{E}_e$ (despite having the same bases) for convenience in partial derivatives, see Appendix B.3.

The effective stress tensor, $\boldsymbol{\phi}$, is given as $\boldsymbol{\phi} = \widehat{\boldsymbol{\tau}}_e - \mathbf{B}$ where $\widehat{\boldsymbol{\tau}}_e$ and $\mathbf{B}$, by their definitions, are functions of $\boldsymbol{\phi}$ through the correction tensor $\Gamma\mathbf{Q}$. This nonlinear equation in terms of $\boldsymbol{\phi}$ is solved iteratively (this implies a secondary Newton-Raphson loop, aside from the loop for $\Delta\gamma$ and Γ, i.e., at constant $\Delta\gamma$ and Γ; also, the order of Newton-Raphson loops within the workflow is irrelevant), and requires a Jacobian derived with respect to $\boldsymbol{\phi}$. To get $\boldsymbol{\phi}$ the equation to be solved is written in terms of the residual tensor $\mathbf{Y}$:

$$\mathbf{Y} \equiv \boldsymbol{\phi} - \widehat{\boldsymbol{\tau}}_e + \mathbf{B} = 0 \,, \tag{B.20}$$

which is solved iteratively to obtain $\boldsymbol{\phi}$ for the i^{th} iteration according to:

$$\Delta\boldsymbol{\phi} = -\left(\frac{\partial \mathbf{Y}}{\partial \boldsymbol{\phi}}\right)^{-1}\Bigg|_{\Delta\gamma,\Gamma} : \mathbf{Y} \,, \tag{B.21}$$

$$\boldsymbol{\phi}_{i+1} = \boldsymbol{\phi}_i + \Delta\boldsymbol{\phi} \,, \tag{B.22}$$

where the Jacobian of the residual, $\frac{\partial \mathbf{Y}}{\partial \boldsymbol{\phi}}\Big|_{\Delta\gamma,\Gamma}$, is derived in the Appendix B.3.

In the primary plasticity loop, the two unknowns $\Delta\gamma$ and Γ are iteratively estimated. The first equation, the extended yield function, $\bar{F}$, with the flow rule parameter is shown below:

$$\bar{F}(\Gamma, \Delta\gamma) = a_2 {\phi_e}^{\alpha} - a_1 \phi_p - a_0 - \left(\eta \frac{\Gamma}{\Delta t}\right)^p = 0 \,. \tag{B.23}$$

The temperature dependency notation is dropped for readability. The second equation is the relation between the two unknowns, Eq. (B.13), enforced as a functional:

$$G(\Gamma, \Delta\gamma) \equiv \Delta\gamma - k\Gamma A = 0 \,, \tag{B.24}$$

where, the scalar A is taken as:

$$A = \sqrt{\mathbf{Q} : \mathbf{Q}} = \sqrt{6\phi_e^2 + \frac{4}{3}\beta^2 \phi_p^2} \,. \tag{B.25}$$

To solve the system of equations, $\bar{F}$ and G, for the unknowns $\Delta\gamma$ and Γ, the derivatives with respect to these variables are required, and are mentioned in Appendix B.4. This system of equations, stated below in its matrix form, is solved iteratively to compute the increments of $\Delta\gamma$ and Γ:

$$\begin{bmatrix} \Delta(\Delta\gamma) \\ \Delta\Gamma \end{bmatrix} = - \begin{bmatrix} \frac{\partial \bar{F}}{\partial \Delta\gamma} & \frac{\partial \bar{F}}{\partial \Gamma} \\ \frac{\partial G}{\partial \Delta\gamma} & \frac{\partial G}{\partial \Gamma} \end{bmatrix}^{-1} \begin{bmatrix} \bar{F} \\ G \end{bmatrix} , \tag{B.26}$$

allowing the final solution to the inner plasticity loop for the j^{th} iteration:

$$\Delta\gamma_{j+1} = \Delta\gamma_j + \Delta(\Delta\gamma) , \tag{B.27}$$

$$\Gamma_{j+1} = \Gamma_j + \Delta\Gamma . \tag{B.28}$$

Appendix B.3. Jacobian of the Effective Stress Residual

Starting from Eq. (B.20), the Jacobian at constant $\Delta\gamma$ and Γ is expressed as follows:

$$\left.\frac{\partial \mathbf{Y}}{\partial \boldsymbol{\phi}}\right|_{\Delta\gamma,\Gamma} = \boldsymbol{\mathcal{I}} - \frac{\partial \widehat{\boldsymbol{\tau}}_e}{\partial \boldsymbol{\phi}} + \frac{\partial \mathbf{B}}{\partial \boldsymbol{\phi}} , \tag{B.29}$$

where, the derivative of $\mathbf{B}$ comes from its solution in Eqs. (B.18) and the flow normal $\mathbf{Q}$ in Eq. (B.9):

$$\frac{\partial \mathbf{B}}{\partial \boldsymbol{\phi}} = \frac{k^2 H_{\mathbf{B}} \Gamma}{C_{\mathbf{B}}} \left(3\boldsymbol{\mathcal{I}}^{dev} + \frac{2\beta}{3}\frac{1}{3}\mathbf{I} \otimes \mathbf{I} \right) + \frac{3}{C_{\mathbf{B}}} \frac{\partial \operatorname{dev} \mathbf{B}^{n*}}{\partial \operatorname{dev} \mathbf{Q}} : \boldsymbol{\mathcal{I}}^{dev} , \tag{B.30}$$

and the derivative of $\widehat{\boldsymbol{\tau}}_e$ is conveniently written in terms of the corrected $\mathbf{E}_e$ as $\frac{\partial \widehat{\boldsymbol{\tau}}_e}{\partial \boldsymbol{\phi}} = \frac{\partial \widehat{\boldsymbol{\tau}}_e}{\partial \mathbf{E}_e} : \frac{\partial \mathbf{E}_e}{\partial \boldsymbol{\phi}}$. The derivative $\frac{\partial \widehat{\boldsymbol{\tau}}_e}{\partial \mathbf{E}_e}$ is the constitutive stiffness matrix developed in [53]. The derivative of $\mathbf{E}_e$ following its corrected relation in Eq. (B.16) reads:

$$\frac{\partial \mathbf{E}_e}{\partial \boldsymbol{\phi}} = -\Gamma \frac{\partial \mathbf{Q}}{\partial \boldsymbol{\phi}} = -3\Gamma \boldsymbol{\mathcal{I}}^{dev} - \frac{2\beta\Gamma}{3}\frac{1}{3}\mathbf{I} \otimes \mathbf{I} . \tag{B.31}$$

Appendix B.4. Partial Derivatives of $\overline{F}$ and G

The derivatives of $G(\Gamma, \Delta\gamma)$, using Eq. (B.24), are as follows:

$$\frac{\partial G}{\partial \Delta\gamma} = 1 - k\Gamma \frac{\partial A}{\partial \Delta\gamma} \quad \text{and} \quad \frac{\partial G}{\partial \Gamma} = -k \left(A + \Gamma \frac{\partial A}{\partial \Gamma} \right) . \tag{B.32}$$

Then, the derivatives of $\bar{F}(\Gamma, \Delta\gamma)$, using Eq. (B.23), read:

$$\frac{\partial \bar{F}}{\partial \Delta\gamma} = H_2 {\phi_e}^{\alpha} + a_2 \alpha {\phi_e}^{\alpha-1} \frac{\partial \phi_e}{\partial \Delta\gamma} - H_1 \phi_p - a_1 \frac{\partial \phi_p}{\partial \Delta\gamma} - H_0 - \frac{1}{\Delta t} \left(\frac{\eta}{\Delta t} \right)^{p-1} p \Gamma^p \frac{\partial \eta}{\partial \Delta\gamma} , \tag{B.33}$$

$$\frac{\partial \bar{F}}{\partial \Gamma} = a_2 \alpha \phi_e^{\alpha-1} \frac{\partial \phi_e}{\partial \Gamma} - a_1 \frac{\partial \phi_p}{\partial \Gamma} - \left(\frac{\eta}{\Delta t} \right)^p p \Gamma^{p-1} . \tag{B.34}$$

In these 4 relations, the derivatives of the invariants ϕ_e and ϕ_p with respect to the unknowns are to be determined. Closed-form expressions of these terms are provided in [53].

Table B.2: Elasto-Plastic Integration Algorithm

```
Given, independent variables at previous and current time-steps: $T^n$,$T$, $\mathbf{F}$, $\mathbf{F}^n$
and internal variables at previous time-step: $\mathfrak{E}_i^n$, $\gamma^n$, $\mathbf{B}^n$, $\widehat{\psi}^n_{\mathrm{max}}$.

  a. Predictor: $\mathbf{F}_p^{\mathrm{pr}}$, $\mathbf{E}_{\mathrm{eff}}^{\mathrm{pr}}$, $\widehat{\boldsymbol{\tau}}_e^{\mathrm{pr}}$, $\boldsymbol{\phi}^{\mathrm{pr}}$ in Eqs. (B.1)-(B.7);
  b. Check Yield Function: $F(\boldsymbol{\phi}^{\mathrm{pr}})$ in Eq. (B.8);
      – IF $F < 0$
          1. Elastic Regime: $(\cdot) = (\cdot)^{\mathrm{pr}} \rightarrow$ Go to Step c.
      – ELSE IF $F \geq 0$
          1. Onset of Plasticity:
              1.1 Solve outer loop: Eq. (B.8) to update $\Delta\gamma$, $\Gamma$ ;
              1.2 Update: Hardening Laws in Eqs. (80)-(86);
              1.3 Update: $\mathbf{Q}$, $\mathbf{E}_e$, $\widehat{\boldsymbol{\tau}}_e$, $\mathbf{B}$, $\boldsymbol{\phi}$ in Section Appendix B.2;
              1.4 Check inner loop: $\mathbf{Y}$ in Eq. (B.20),
              · IF $||\mathbf{Y}|| \leq tol$
                  1.4.1 Exit Loop: Go to Step 1.6;
              · ELSE IF $||\mathbf{Y}|| > tol$
                  1.4.2 Solve inner loop: Eq. (B.21) to update $\boldsymbol{\phi}$;
                  1.4.3 Corrector: $\mathbf{Q}$, $\mathbf{E}_e$, $\widehat{\boldsymbol{\tau}}_e$, $\mathbf{B}$ in Section Appendix B.2;
                  1.4.4 Condition: IF $||\mathbf{Y}|| < tol \rightarrow$ Go to Step 1.6, else repeat Step 1.4.2;
              1.5 Update extended yield: $\bar{F}$ in Eq. (B.23);
              1.6 Condition: IF $\bar{F} \leq tol \rightarrow$ Go to Step c., else repeat Step 1.1;
      – END IF
  c. Update: $\mathbf{F}_p$ in Appendix B.2 and $\widehat{\mathbf{P}}$ in Eq. (88).
  d. Update: Tangent operators in Appendix C.
```

Appendix C. Effective Material Tangent Operators

The effective tangent operators for the 1^{st} PK stress ($\mathbf{P}$), heat flux ($\boldsymbol{Q}$) and heat source (W_M) are briefly presented here. For the full development of the closed form expressions, refer to [53].

Appendix C.1. 1^{st} PK Stress

From Eq. (88), the tangents of $\mathbf{P}$ with respect to $\mathbf{F}$ and T in a (pseudo-)damaged state are given below:

$$\frac{\partial \mathbf{P}}{\partial \mathbf{F}} = \frac{\partial \widehat{\mathbf{P}}}{\partial \mathbf{F}} \zeta + \widehat{\mathbf{P}} \otimes \frac{\partial \zeta}{\partial \mathbf{F}} \quad \text{and} \quad \frac{\partial \mathbf{P}}{\partial T} = \frac{\partial \widehat{\mathbf{P}}}{\partial T} \zeta + \widehat{\mathbf{P}} \frac{\partial \zeta}{\partial T} \,, \tag{C.1}$$

where the terms $\frac{\partial \widehat{\mathbf{P}}}{\partial \mathbf{F}}$ and $\frac{\partial \widehat{\mathbf{P}}}{\partial T}$ are the mechanical and thermal tangents of $\widehat{\mathbf{P}}$ in the undamaged state. Using Eq. (88), they are explicitly stated below:

$$\begin{aligned} \frac{\partial \widehat{\mathbf{P}}}{\partial \mathbf{F}} &= \frac{\partial \mathbf{F}_e}{\partial \mathbf{F}} {}^{2}\!\cdot \left(\widehat{\mathbf{S}}_e \cdot \mathbf{F}_p^{-T} \right) + \mathbf{F}_e \cdot^{1} \frac{\partial \widehat{\mathbf{S}}_e}{\partial \mathbf{F}} {}^{2}\!\cdot \mathbf{F}_p^{-T} + \left(\mathbf{F}_e \cdot \widehat{\mathbf{S}}_e \right) \cdot \frac{\partial \mathbf{F}_p^{-T}}{\partial \mathbf{F}} \,, & \text{(C.2)} \\ \frac{\partial \widehat{\mathbf{P}}}{\partial T} &= \frac{\partial \mathbf{F}_e}{\partial T} \cdot \left(\widehat{\mathbf{S}}_e \cdot \mathbf{F}_p^{-1} \right) + \mathbf{F}_e \cdot \frac{\partial \widehat{\mathbf{S}}_e}{\partial T} \cdot \mathbf{F}_p^{-1} + \left(\mathbf{F}_e \cdot \widehat{\mathbf{S}}_e \right) \cdot \frac{\partial \mathbf{F}_p^{-1}}{\partial T} \,, & \text{(C.3)} \end{aligned}$$

where in the 1^{st} equation, the superscripts $({}^{i}\cdot)$ and $(\cdot^{i})$ imply tensor dot product operations with the i^{th} index of the tensor on the left and tensor on the right, respectively. Then follow the derivatives of $\widehat{\mathbf{S}}_e$ using its relation with $\widehat{\boldsymbol{\tau}}_e$:

$$\frac{\partial \widehat{\mathbf{S}}_e}{\partial \mathbf{F}} = \frac{\partial \widehat{\boldsymbol{\tau}}_e}{\partial \mathbf{F}} {}^{1,2}\!:^{1,2} \boldsymbol{\mathcal{L}}_e + \widehat{\boldsymbol{\tau}}_e :^{1,2} \frac{\partial \boldsymbol{\mathcal{L}}_e}{\partial \mathbf{F}} \quad \text{and} \quad \frac{\partial \widehat{\mathbf{S}}_e}{\partial T} = \frac{\partial \widehat{\boldsymbol{\tau}}_e}{\partial T} :^{1,2} \boldsymbol{\mathcal{L}}_e + \widehat{\boldsymbol{\tau}}_e :^{1,2} \frac{\partial \boldsymbol{\mathcal{L}}_e}{\partial T} \,. \tag{C.4}$$

The 4^{th} order tensor $\boldsymbol{\mathcal{L}}_e = \frac{\partial \ln \mathbf{C}_e}{\partial \mathbf{C}_e} = \boldsymbol{\mathcal{I}}\,{}^{2}\!\cdot^{1} \mathbf{C}_e{}^{-1}$ and its derivative with $\mathbf{C}_e$, $\frac{\partial \boldsymbol{\mathcal{L}}_e}{\partial \mathbf{C}_e} = -\boldsymbol{\mathcal{I}}\,{}^{2}\!\cdot^{1} \boldsymbol{\mathcal{I}}\,{}^{2}\!\cdot^{1} \mathbf{C}_e^{-1} \cdot \mathbf{C}_e^{-1}$, with $\boldsymbol{\mathcal{I}}$ being the 4^{th} order symmetric identity tensor, stem from the definition of log strain $\mathbf{E}_e$.

Appendix C.2. Heat Flux Derivatives

Thermal conductivity is taken as a scalar (χ) which is in line with the assumption of isotropy. The derivatives of the thermal flux in the reference configuration using Eq. (14) are estimated as:

$$\frac{\partial \boldsymbol{Q}}{\partial T} = \frac{1}{\chi} \boldsymbol{Q} \frac{\partial \chi}{\partial T} \,, \quad \frac{\partial \boldsymbol{Q}}{\partial \boldsymbol{H}} = -J \chi \mathbf{C}^{-1} \,, \quad \text{and} \quad \frac{\partial \boldsymbol{Q}}{\partial \mathbf{F}} = \frac{\boldsymbol{Q}}{J} \otimes \frac{\partial J}{\partial \mathbf{F}} - J \chi \frac{\partial \mathbf{C}^{-1}}{\partial \mathbf{F}} {}^{2}\!\cdot \boldsymbol{H} \,, \tag{C.5}$$

where $J = \det \mathbf{F}$ is the Jacobian of the deformation, $\otimes$ in the last equation is intended in a manner to produce a 3^{rd} order tensor.

Appendix C.3. Mechanical Source Derivatives

The mechanical heat source in Eq. (90) is differentiated as follows:

$$\begin{aligned} \frac{\partial W_M}{\partial \mathbf{F}} &= \frac{\partial \zeta}{\partial \mathbf{F}} \left(-C_p \dot{T} + \boldsymbol{\phi} : \mathbf{D}_p - R \dot{\gamma} \right) + \zeta \left(\left(\frac{\partial \boldsymbol{\phi}}{\partial \mathbf{C}_e^{\text{pr}}} : \frac{\partial \mathbf{C}_e^{\text{pr}}}{\partial \mathbf{F}} \right) {}^{1,2}\!: \mathbf{D}_p + \boldsymbol{\phi} : \frac{\partial \mathbf{D}_p}{\partial \mathbf{F}} \right) \;... \\ &\quad ... \; + \zeta \left(-\frac{\partial R}{\partial \gamma} \frac{\partial \gamma}{\partial \mathbf{F}} \dot{\gamma} - \frac{R}{\Delta t} \frac{\partial \gamma}{\partial \mathbf{C}_e^{\text{pr}}} : \frac{\partial \mathbf{C}_e^{\text{pr}}}{\partial \mathbf{F}} \right) - \frac{\partial^2 \psi}{\partial \widehat{\psi}_{\max} \partial \mathbf{F}} \dot{\widehat{\psi}}_{\max} - \frac{\partial \psi}{\partial \widehat{\psi}_{\max}} \frac{1}{\Delta t} \frac{\partial \widehat{\psi}_{\max}}{\partial \mathbf{F}} \,, \\ \frac{\partial W_M}{\partial T} &= \frac{\partial \zeta}{\partial T} \left(-C_p \dot{T} + \boldsymbol{\phi} : \mathbf{D}_p - R \dot{\gamma} \right) \; + \zeta \left(-\frac{C_p}{\Delta t} + \frac{\partial \boldsymbol{\phi}}{\partial T} : \mathbf{D}_p + \boldsymbol{\phi} : \frac{\partial \mathbf{D}_p}{\partial T} \right) \;... \\ &\quad ... \; + \zeta \left(- \left(\frac{\partial R}{\partial T} + \frac{\partial R}{\partial \gamma} \frac{\partial \gamma}{\partial T} \right) \dot{\gamma} - \frac{R}{\Delta t} \frac{\partial \gamma}{\partial T} \right) - \frac{\partial^2 \psi}{\partial \widehat{\psi}_{\max} \partial T} \dot{\widehat{\psi}}_{\max} - \frac{\partial \psi}{\partial \widehat{\psi}_{\max}} \frac{1}{\Delta t} \frac{\partial \widehat{\psi}_{\max}}{\partial T} \,, \end{aligned} \tag{C.6}$$

where the expressions of the derivatives are fully derived in [53].

Appendix D. Identified Parameters

Table D.3: Relaxation spectrum of Polypropylene BJ380MO in the temperature range of -20 to 70°C containing 27 Maxwell branches, $T_{\text{ref}} = 20°\text{C}$.

i	E_i (MPa)	$\log_{10}(e_i(s))$	i	E_i (MPa)	$\log_{10}(e_i(s))$
∞	380.0000	-	14	67.2217	-2
1	127.0091	-15	15	67.1576	-1
2	124.3750	-14	16	67.6598	0
3	119.8748	-13	17	72.8265	1
4	116.2080	-12	18	78.6874	2
5	112.2114	-11	19	82.5223	3
6	108.6439	-10	20	86.7273	4
7	103.3254	-9	21	85.0493	5
8	107.5228	-8	22	85.9975	6
9	100.8965	-7	23	80.5892	7
10	91.8305	-6	24	85.6877	8
11	83.5821	-5	25	69.0003	9
12	79.5660	-4	26	50.0000	10
13	71.5896	-3	27	218.5649	11

Table D.4: Quasi-Nonlinear TVE parameters of Polypropylene BJ380MO in the temperature range of -20 to 70°C for 27 Maxwell branches.

i	V_{t1}, D_{t1}	V_{t2}, D_{t2}	V_{t3}, D_{t3}	C_i	V_{c1}, D_{c1}	V_{c2}, D_{c2}	V_{c3}, D_{c3}
∞	1,000.000	1.500	0.000	1.800	2,000.000	1.350	0.000
1	5,000.000	0.500	0.000	5.000	40,000.000	1.500	1.000
2	5,384.615	0.500	0.000	4.754	37,576.923	1.481	0.931
3	5,769.231	0.500	0.000	4.508	35,153.846	1.462	0.862
4	6,153.846	0.500	0.000	4.262	32,730.769	1.442	0.792
5	6,538.462	0.500	0.000	4.015	30,307.692	1.423	0.723
6	6,923.077	0.500	0.000	3.769	27,884.615	1.404	0.654
7	7,307.692	0.500	0.000	3.523	25,461.538	1.385	0.585
8	7,692.308	0.500	0.000	3.277	23,038.462	1.365	0.515
9	8,076.923	0.500	0.000	3.031	20,615.385	1.346	0.446
10	8,461.538	0.500	0.000	2.785	18,192.308	1.327	0.377
11	8,846.154	0.500	0.000	2.538	15,769.231	1.308	0.308
12	9,230.769	0.500	0.000	2.292	13,346.154	1.288	0.238
13	9,615.385	0.500	0.000	2.046	10,923.077	1.269	0.169
14	10,000.000	0.500	0.000	1.800	8,500.000	1.250	0.100
15	10,000.000	0.500	0.000	1.800	8,500.000	1.250	0.100
16	9,291.667	0.521	0.004	1.800	8,166.667	1.258	0.096
17	8,583.333	0.542	0.008	1.800	7,833.333	1.267	0.092
18	7,875.000	0.562	0.013	1.800	7,500.000	1.275	0.088
19	7,166.667	0.583	0.017	1.800	7,166.667	1.283	0.083
20	6,458.333	0.604	0.021	1.800	6,833.333	1.292	0.079
21	5,750.000	0.625	0.025	1.800	6,500.000	1.300	0.075
22	5,041.667	0.646	0.029	1.800	6,166.667	1.308	0.071
23	4,333.333	0.667	0.033	1.800	5,833.333	1.317	0.067
24	3,625.000	0.688	0.037	1.800	5,500.000	1.325	0.062
25	2,916.667	0.708	0.042	1.800	5,166.667	1.333	0.058
26	2,208.333	0.729	0.046	1.800	4,833.333	1.342	0.054
27	1,500.000	0.750	0.050	1.800	4,500.000	1.350	0.050

Table D.5: Thermoviscoplastic parameters for Polypropylene BJ380MO (PP) at reference temperature 20°C.

TVP Parameters at $T_{\text{ref}} = 20°\text{C}$	PP
Compressive yield stress (σ_c) in MPa	$28.9 + 5.19\gamma + 5.19\left(1 - e^{-30\gamma}\right)$
Tensile yield stress (σ_t) in MPa	$9.43 + 5.13\left(1 - e^{-15\gamma}\right)$
Kinematic Hardening Modulus ($H_{\mathbf{B}}$) in MPa	–
Power yield exponent (α)	1.5
Plastic Poisson's ratio (ν_p)	0.4
Rate sensitivity exponent (p)	0.21
Viscosity coefficient (η) in MPa · s	5388.03

Table D.6: Dimensionless temperature functions for Polypropylene BJ380MO (PP) with $T_{\text{ref}} = 20°\text{C}$.

Temperature functions	PP
Compressive yield stress ($a_{T_\gamma}{}^{c}$)	$\exp\left(-0.0123(T - T_{\text{ref}})\right)$
Tensile yield stress ($a_{T_\gamma}{}^{t}$)	$\exp\left(-0.00842(T - T_{\text{ref}})\right)$
Viscosity coefficient (a_{T_η})	$\exp\left(-0.02055(T - T_{\text{ref}})\right)$

Table D.7: Thermal material parameters for Polypropylene BJ380MO (PP) at room temperature 23°C.

Parameter	PP
Thermal Conductivity (χ) in $Wm^{-1}K^{-1}$	0.14
Coefficient of thermal expansion (α_∞) in K^{-1}	6 x 10^{-5}
Specific heat per unit volume (C_p) in $JK^{-1}m^{-3}$	1.7195 x 10^{6}

Table D.8: Relaxation spectrum of TPU EOS 1301 in the temperature range of -30 to 120°C containing 27 Maxwell branches.

i	E_i (MPa)	$\log_{10}(e_i(s))$	i	E_i (MPa)	$\log_{10}(e_i(s))$
∞	29.4908	-	14	7.7437	12
1	237.9701	-1	15	6.8576	13
2	91.1210	0	16	5.9778	14
3	75.2960	1	17	5.3304	15
4	56.9817	2	18	4.7286	16
5	44.0985	3	19	4.2352	17
6	33.9610	4	20	3.8626	18
7	26.5513	5	21	3.4947	19
8	21.0939	6	22	3.1872	20
9	17.1109	7	23	3.0166	21
10	14.1270	8	24	2.7892	22
11	11.9419	9	25	2.7253	23
12	10.1674	10	26	2.4773	24
13	8.7719	11	27	3.0768	25

Table D.9: Quasi-Nonlinear TVE parameters of TPU EOS 1301 in the temperature range of -30 to 120°C for all Maxwell branches.

QNL TVE Parameters - TPU	
$V_{t1}, V_{c1}, D_{t1}, D_{c1}$	150
$V_{t2}, V_{c2}, D_{t2}, D_{c2}$	0.75
V_{t3}, D_{t3}	8.5
V_{c3}, D_{c3}	0.15
V_{t4}, D_{t4}	0.75
V_{c4}, D_{c4}	1.
V_{t5}, D_{t5}	0.028
V_{c5}, D_{c5}	0.

Table D.10: Thermoviscoplastic parameters for TPU EOS 1301 at room temperature 23°C.

Parameters at $T = 23$°C	TPU
Compressive yield stress (σ_c) in MPa	$4.5 + 5\gamma + 5.\left(1 - e^{-5\gamma}\right)$
Tensile yield stress (σ_t) in MPa	$4.5 + 5\gamma + 7.5\left(1 - e^{-12.5\gamma}\right)$
Kinematic Hardening Modulus ($H_{\mathbf{B}}$) in MPa	$20 + 25\gamma$
Power yield exponent (α)	3
Plastic Poisson's ratio (ν_p)	0.4
Rate sensitivity exponent (p)	0.21
Viscosity coefficient (η) in MPa · s	1000

Table D.11: Thermal material parameters for TPU EOS 1301 at room temperature 23°C.

Parameter	TPU
Thermal Conductivity (χ) in $Wm^{-1}K^{-1}$	0.2332
Coefficient of thermal expansion (α_∞) in K^{-1}	1.5 x 10^{-4}
Specific heat per unit volume (C_p) in $JK^{-1}m^{-3}$	2.0535 x 10^{6}